



ISTITUTO NAZIONALE DI RICERCA METROLOGICA Repository Istituzionale

Investigating the relationship between AGN activity and stellar mass in zCOSMOS galaxies at $0 < z < 1$ using emission-line diagnostic diagrams

Original

Investigating the relationship between AGN activity and stellar mass in zCOSMOS galaxies at $0 < z < 1$ using emission-line diagnostic diagrams / Vitale, M.; Mignoli, M.; Cimatti, A.; Lilly, S. J.; Carollo, C. M.; Contini, T.; Kneib, J. -P.; Le Fevre, O.; Mainieri, V.; Renzini, A.; Scodeggio, M.; Zamorani, G.; Bardelli, S.; Barnes, L.; Bolzonella, M.; Bongiorno, A.; Bordoloi, R.; Bschorr, T. J.; Cappi, A.; Caputi, K.; Coppa, G.; Cucciati, O.; de la Torre, S.; de Ravel, L.; Franzetti, P.; Garilli, B.; Iovino, A.; Kampczyk, P.; Knobel, C.; Koekemoer, A. M.; Kovalev, K.; Lamareille, F.; Le Borgne, J. -F.; Le Brun, V.; López-Sanjuan, C.; Maier, C.; Mccracken, H. J.; Moresco, M.; Nair, P.; Oesch, B.; Paoletti, P.; Pentericci, A.; Pozzetti, L.; Presotto, V.; Silverman, J.; Tanaka, M.; Tasca, L.; Tresse, L.; Vergani, D.; Welikala, N.; Zucca, E.. - In: ASTRONOMY & ASTROPHYSICS. - ISSN 0004-6361. - 556:(2013), p. A11. [10.1051/0004-6361/201220258]

Publisher:

EDP SCIENCES S A

Published

DOI:10.1051/0004-6361/201220258

Terms of use:

This article is made available under terms and conditions as specified in the corresponding bibliographic description in the repository

Publisher copyright

(Article begins on next page)

Investigating the relationship between AGN activity and stellar mass in zCOSMOS galaxies at $0 < z < 1$ using emission-line diagnostic diagrams[★]

M. Vitale^{1,2,3}, M. Mignoli⁴, A. Cimatti³, S. J. Lilly⁵, C. M. Carollo⁵, T. Contini^{6,7}, J.-P. Kneib⁸, O. Le Fevre⁸, V. Mainieri⁹, A. Renzini¹⁰, M. Scodeggio¹¹, G. Zamorani⁴, S. Bardelli⁴, L. Barnes⁵, M. Bolzonella⁴, A. Bongiorno¹², R. Bordoloi⁵, T. J. Bschorr⁵, A. Cappi⁴, K. Caputi²¹, G. Coppola¹², O. Cucciati¹³, S. de la Torre¹⁴, L. de Ravel¹⁴, P. Franzetti¹¹, B. Garilli¹¹, A. Iovino¹³, P. Kampczyk⁵, C. Knobel⁵, A. M. Koekemoer¹⁷, K. Kovač⁵, F. Lamareille^{6,7}, J.-F. Le Borgne^{6,7}, V. Le Brun⁸, C. López-Sanjuan⁸, C. Maier^{5,20}, H. J. McCracken¹⁸, M. Moresco³, P. Nair⁴, P. A. Oesch^{5,21}, R. Pello^{6,7}, Y. Peng⁵, E. Pérez Montero^{6,7,15}, L. Pozzetti⁴, V. Presotto¹³, J. Silverman¹⁶, M. Tanaka¹⁶, L. Tasca⁸, L. Tresse⁸, D. Vergani²³, N. Welikala¹⁹, and E. Zucca⁴

¹ I. Physikalisches Institut, Universität zu Köln, Zùlpicher Strasse 77, 50937 Köln, Germany e-mail: vitale@ph1.uni-koeln.de

² Max-Planck Institut für Radioastronomie, Auf dem Hügel 69, 53121 Bonn, Germany

³ Dipartimento di Astronomia, Università di Bologna, via Ranzani 1, 40127 Bologna, Italy

⁴ INAF – Osservatorio Astronomico di Bologna, via Ranzani 1, 40127 Bologna, Italy

⁵ Institute for Astronomy, ETH Zurich, 8093 Zurich, Switzerland

⁶ Institut de Recherche en Astrophysique et Planétologie, CNRS, 14 avenue Édouard Belin, 31400 Toulouse, France

⁷ IRAP, Université de Toulouse, UPS-OMP, 31400 Toulouse, France

⁸ Aix-Marseille Université, CNRS, LAM (Laboratoire d'Astrophysique de Marseille) UMR 7326, 13388 Marseille, France

⁹ European Southern Observatory, 85748 Garching, Germany

¹⁰ INAF – Osservatorio Astronomico di Padova, Vicolo dell'Osservatorio 5, 35122 Padova, Italy

¹¹ INAF – IASF Milano, 20133 Milano, Italy

¹² Max-Planck Institut für Extraterrestrische Physik, 85748 Garching, Germany

¹³ INAF Osservatorio Astronomico di Brera, 20133 Milan, Italy

¹⁴ Institute for Astronomy, University of Edinburgh, Royal Observatory, Edinburgh, EH93HJ, UK

¹⁵ Instituto de Astrofísica de Andalucía, CSIC, Apartado de Correos 3004, 18080 Granada, Spain

¹⁶ Kavli Institute for the Physics and Mathematics of the Universe (WPI), Todai Institutes for Advanced Study, The University of Tokyo, 5-1-5 Kashiwanoha, 277-8583 Kashiwa, Japan

¹⁷ Space Telescope Science Institute, Baltimore, MD 21218, USA

¹⁸ Institut d'Astrophysique de Paris, UMR 7095 CNRS, Université Pierre & Marie Curie, 75014 Paris, France

¹⁹ Institut d'Astrophysique Spatiale, Bâtiment 121, Université Paris-Sud XI & CNRS, 91405 Orsay Cedex, France

²⁰ Department of Astronomy, University of Vienna, Tuerkenschanzstrasse 17, 1180 Vienna, Austria

²¹ Kapteyn Astronomical Institute, University of Groningen, PO Box 800, 9700 AV Groningen, The Netherlands

²² UC Santa Cruz/UCO Lick Observatory, 1156 High Street, Santa Cruz, CA 95064, USA

²³ INAF – IASF Bologna, via P. Gobetti 101, 40129 Bologna, Italy

Received 19 August 2012 / Accepted 13 February 2013

ABSTRACT

Context. Active galactic nuclei (AGN) are thought to play an important role in galaxy evolution. It has been suggested that AGN feedback could be partly responsible for quenching star-formation in the hosts, leading to transition from the blue cloud to the red sequence. The transition seems to occur faster for the most massive galaxies, where traces of AGN activity have been found as early as at $z < 0.1$. The correlation between AGN activity, aging of the stellar populations, and stellar mass still needs to be fully understood, especially at high redshifts.

Aims. Our aim is to investigate the link between AGN activity, star-formation, and stellar mass of the host galaxy at $0 < z < 1$, looking for spectroscopic traces of AGN and aging of the host. This work provides an extension of the existing studies at $z < 0.1$ and contributes to shed light on galaxy evolution at intermediate redshifts.

Methods. We used the zCOSMOS 20k data to create a sample of galaxies at $z < 1$. We divided the sample into several mass-redshift bins to obtain stacked galaxy spectra with an improved signal-to-noise ratio (S/N). We exploited emission-line diagnostic diagrams to separate AGN from star-forming galaxies.

Results. We found an indication of a role for the total galaxy stellar mass in leading galaxy classification. Stacked spectra show AGN signatures above the $\log M_*/M_\odot > 10.2$ threshold. Moreover, the stellar populations of AGN hosts are found to be older than star-forming and composite galaxies. This could be due to the tendency of AGN to reside in massive hosts.

Conclusions. The dependence of the AGN classification on the stellar mass agrees with what has been found in previous research. Together with the evidence of older stellar populations inhabiting the AGN-like galaxies, it is consistent with the downsizing scenario. In particular, our evidence points to an evolutionary scenario where the AGN-feedback is capable of quenching the star formation in the most massive galaxies. Therefore, the AGN-feedback is the best candidate for initiating the passive evolutionary phase of galaxies.

Key words. galaxies: active – galaxies: evolution – galaxies: starburst – galaxies: stellar content

[★] Appendices are available in electronic form at <http://www.aanda.org>

1. Introduction

In recent years, a better overview of galaxy formation and evolution has been developing, with a great contribution coming from large cosmic surveys. In particular, the local galaxy's colour function has been discovered to be a bimodal function (Strateva et al. 2001; Kauffmann et al. 2003; Baldry et al. 2004; Balogh et al. 2004; Hogg et al. 2004). The two dominant sequences are associated with the ellipticals+S0s population (red distribution, or red sequence) and the spirals+irregulars population (blue distribution, or blue cloud), while galaxies showing intermediate properties are considered as composites or transitional objects (green valley). Early-type galaxies (ETGs) dominate at the top-end of the local galaxy mass function where, conversely, late-type galaxies (LTGs) become progressively more rare. Discovering that the black-hole (BH) mass strongly correlates with the properties of the hosting galaxies (Magorrian et al. 1998; Ferrarese & Merritt 2000) has generated new hypotheses in linking the BH growth with galaxy formation and evolution. The mass of the host seems to play a key role in the latter process as well. According to the “downsizing” scenario (Cowie et al. 1996; Kodama et al. 2004; Thomas et al. 2005; Tanaka et al. 2005; Juneau et al. 2005; Bundy et al. 2006), the sites of active star formation include high-mass galaxies at high redshift ($z \gtrsim 1$) but only intermediate- and low-mass galaxies at $z \lesssim 1$. This scenario is supported by several studies; it has been found, for instance, that luminous and massive spheroidals build up most of their stellar mass prior to $z \approx 1$, while low-mass ellipticals continue to grow after this cosmic time (Heavens et al. 2004; Treu et al. 2005; van der Wel et al. 2005; Jimenez et al. 2005). Downsizing may be a natural expectation in a hierarchical galaxy formation scenario, provided that there is a mechanism that quenches star formation at earlier times in massive galaxies. As a support to downsizing and the link between mass and galaxy evolution, Bundy et al. (2004) found that the relative abundance of red galaxies with intermediate mass ($M \approx 6 \times 10^{10} M_{\odot}$) increases by a factor of 3 from $z \sim 1.2$ to $z \sim 0.55$, while the number of blue late-type galaxies declines significantly.

The fast suppression of the star formation activity (quenching) is currently thought to initiate passive galaxy evolution and to be largely responsible for the growing abundance of galaxies on the red sequence (Faber et al. 2007). The quenching mass (M_Q), namely the stellar mass above which galaxies start their passive phase, has been found to be a function of the redshift (Bundy et al. 2004). Blue and star-forming galaxies at their quenching mass are redder than the average blue population, suggesting a transition from blue- to red-type galaxies.

The star formation quenching could be explained by several mechanisms. The observed decline of the galaxy star formation from $z \sim 1$ to $z = 0$ can be caused by a gradual gas exhaustion (Cooper et al. 2008). Another mechanism that could explain the quenching are major mergers. The interaction between a galaxy and its neighbors could indeed produce gravitational torques on the gas, reducing its angular momentum and sending it toward the galactic center after an initial starburst phase (Martig et al. 2009). As a result, fuel is available for accretion, allowing the growth of the central BH instead of the formation of new stars in the disk. However, it has been established that mergers cannot be the main cause of the build-up of the galaxy bimodality, since luminous and massive old galaxies formed by this process were already common at $z \sim 1$ (Conselice et al. 2007) and their number density only declines above this value. If merger events

were efficient in forming galaxies at $z < 1$, we would expect an increasing number of massive objects at low redshift, which has not been observed. Similarly, a role for active galactic nuclei (AGN) has been suggested (Ciotti & Ostriker 1997; Binney 2004; Silk 2005; Springel et al. 2005). BHs are thought to be a basic constituent of most massive systems (Richstone et al. 1998) and they have also been identified in some late-type and dwarf galaxies (Filippenko & Ho 2003). During the BH accretion, AGN release a large amount of energy, which could be partially absorbed by the host galaxy to quench the star formation and eventually transform blue galaxies into red galaxies (e.g. Silk & Rees 1998; Croton et al. 2006; Narayanan et al. 2008). According to some calculations (Cattaneo et al. 2009), even a small fraction ($<1\%$) of the energy released within a bulge during the BH accretion would be sufficient to heat and/or blow away the entire gas content. Consistent with this framework, Hopkins et al. (2006) further developed the Sanders et al. (1988) scenario, in which starburst, quasar active phase, BH growth, and elliptical galaxies are connected to each other in a galaxy evolutionary sequence and the gas consumption is coupled with supernova-driven winds and/or AGN-feedback to quench the star formation.

The hypothesis of the AGN-feedback is strengthened by the fact that a large amount of galaxies have been found to go through an active phase. Summed over all Hubble types, roughly half of all galaxies can be considered as active (Ho et al. 1997a), even though some of them show a fairly low activity level. The amount of active galaxies becomes more remarkable for galaxies with a prominent bulge component, rising to 50–70% for Hubble types E-Sb, whereas the detection rate of AGN drops toward later Hubble types (Sc and later), where about 80% of the galaxies host a star-forming nucleus instead. This suggests a clear dependence of nuclear activity on the Hubble type (Kauffmann et al. 2003; Miller et al. 2003). The observed distribution of Hubble types for galaxies hosting active versus inactive nuclei leads to the expectation that the blue and red populations could have not only different nuclear, but also global properties. In particular, it seems that the observed high fraction of AGN in the green valley points to the connection between the end of the star formation phase, observed in a change of the galaxy color, and the rise of AGN activity (Silverman et al. 2009; Schawinski et al. 2010).

AGN can be identified by a variety of methods: an unusually blue continuum, strong radio or X-ray emission, and strong or broad emission lines. In nearby galaxies hosting low-luminosity AGN, we expect the non-stellar signal of the nucleus to be weak with respect to the one coming from the host galaxy, thus one of the best and least biased methods to search for AGN is to conduct a spectroscopic survey of a complete, optical-flux-limited sample of galaxies and study their spectral properties. The line-emitting gas in AGN and star-forming galaxies (SFGs) is powered by two different ionizing mechanisms, producing different emission line ratios: accretion around BH and photoionization by hot massive OB stars. It is important to note that emission lines in narrow-line AGN have a considerably great ionization range and that low-ionization lines are stronger than in normal star-forming galaxies. It has been demonstrated that ordinary O-type stars do not produce sufficiently strong low-ionization lines, accounting for the observed spectra, because they only account for a low percentage of the total blue light at most (Sarzi et al. 2005). Therefore, photoionization arising from a powerful central non-thermal source is the ideal candidate for explaining the excitation mechanism in galaxies that display strong low-ionization emission-lines (Ho 2005).

Emission-line diagnostic diagrams (Baldwin et al. 1981; Veilleux & Osterbrock 1987; Kewley et al. 2003; Lamareille et al. 2004; Lamareille 2010) represent a powerful tool for probing the nature of the dominant ionizing source in galaxies, hence for distinguishing between objects dominated by star formation and galaxies where the nuclear activity is more relevant. Narrow-line AGN can be identified in spectroscopic galaxy surveys by the ratio of some distinctive emission-lines, such as [NII] $\lambda 6583$ Å (hereafter [NII]) or [SII] $\lambda 6717, 31$ Å (hereafter [SII], referring to the combined luminosity of the doublet) over H α $\lambda 6563$ Å and [OIII] $\lambda 5007$ Å over H β $\lambda 4861$ Å (hereafter H α , [OIII] and H β , respectively). The lines that appear in the reddest part of the spectrum are shifted out of the visible wavelength range for $z \gtrsim 0.5$. In this case, it is possible to use the [OII] $\lambda 3726, 29$ Å line (hereafter [OII]) instead (Rola et al. 1997; Lamareille et al. 2004; Pérez-Montero et al. 2007), which is optically visible up to $z \sim 1$.

The aim of this work is to investigate whether it is possible to highlight some evidence of AGN activity in suppressing star formation, with a particular focus on a possible trend of the galaxy total stellar mass. This attempt has been previously made at low-redshift ($z < 0.1$) and the analysis is now extended to redshift up to $z \sim 1$. Kauffmann et al. (2003) found, by using Sloan Digital Sky Survey (SDSS) data, that galaxies divide into two distinct families at a stellar mass threshold of $3 \times 10^{10} M_{\odot}$. The least-massive galaxies show young stellar populations and the low concentrations typical of LTGs. As the stellar mass increases, galaxies show older stellar populations and higher concentrations, typical of ETGs. By using emission-line diagnostic diagrams, Kauffmann and collaborators showed a dependence of the AGN-detection rate on mass, although the authors warned that many objects are classified as “composites” (contributions to the emission-line spectrum come from both star formation and AGN) because of the large size of the SDSS fiber, which can collect up to 40% of the total light from the galaxy. Blue star-forming objects have been found to have masses at the low end of the mass function, while the majority of the ETGs lie at the high end of the mass function (Baldry et al. 2004; Schawinski et al. 2007). Very recently, however, Aird et al. (2012) argued that the finding of more AGN in massive hosts is due to selection effects. These seem to be driven by the Eddington-ratio distribution of AGN in galaxies of any stellar mass. In particular, AGN are more easily detected in massive hosts because sources accreting at low Eddington rate are more luminous than in less massive hosts.

We analyze the evolution of galaxy spectral properties up to $z \sim 1$ by using galaxies from the zCOSMOS-Bright 20k sample (Lilly et al. 2007). With the large number ($\sim 2 \times 10^4$) of observed objects, we are able to measure emission lines from high S/N stacked spectra. The paper is organized as follows. In Sect. 2 we present the zCOSMOS survey and the sample selection. In Sect. 3 we present the spectral analysis of the stacked, stellar-continuum-subtracted galaxy spectra. In Sect. 4 we exploit a set of classical and more recent diagnostic diagrams to identify the main ionizing process inside galaxies and look for a trend of the stellar mass. Section 5 contains our results and discussion. Main findings and conclusions are presented in Sect. 6.

2. Data

2.1. COSMOS and zCOSMOS surveys

The COSMOS survey is a large HST-ACS survey, with *I*-band exposures down to $I_{AB} = 28$ on a field of 2 deg^2

(Scoville et al. 2007). The COSMOS field has been the object of extensive multi-wavelength ground- and space-based observations spanning the entire spectrum: X-ray, UV, optical/NIR, mid-infrared, mm/submillimeter, and radio, providing fluxes measured over 30 bands (Hasinger et al. 2007; Taniguchi et al. 2007; Capak et al. 2007; Lilly et al. 2007; Sanders et al. 2007; Bertoldi et al. 2007; Schinnerer et al. 2007; Koekemoer et al. 2007; McCracken et al. 2010).

The zCOSMOS survey was planned to provide high-quality redshift information to the COSMOS field (Lilly et al. 2007). It benefitted of ~ 600 h of observations at VLT using the VIMOS spectrograph and consists of two parts: zCOSMOS-bright and zCOSMOS-deep. The zCOSMOS-deep targets $\sim 10\,000$ galaxies within the central 1 deg^2 of the COSMOS field, selected through color criteria to have $1.4 \lesssim z \lesssim 3.0$. The zCOSMOS-bright is purely magnitude-limited and covers the whole area of 1.7 deg^2 of the COSMOS field. It provides redshifts for $\sim 20\,000$ galaxies down to $I_{AB} \lesssim 22.5$ as measured from the HST-ACS imaging. The success rate in redshift measurements is very high, 95% in the redshift range $0.5 < z < 0.8$, and the velocity accuracy is $\sim 100 \text{ km s}^{-1}$ (Lilly et al. 2009). Each observed object has been assigned a flag according to the reliability of its measured redshift. Classes 3.x, 4.x redshifts, plus Classes 1.5, 2.4, 2.5, 9.3, and 9.5 are considered a secure set, with an overall reliability of 99% (see Lilly et al. 2009, for details).

Our work is based on the the zCOSMOS-bright survey final release: the so-called 20k sample, totaling 16 623 galaxies with $z \lesssim 2$ and secure redshifts according to the above flag classification. It includes 18 206 objects in total, including stars.

For objects brighter than $I_{AB} = 22.5$ and without secure spectroscopic redshift, photometric data from the COSMOS survey provide good-quality photometric redshifts (Ilbert et al. 2009). Based on a comparison with the zCOSMOS spectroscopic redshifts, Ilbert et al. (2009) estimated an accuracy of $\sigma_{\text{zphot}} = 0.007 \times (1 + z_s)$ for galaxies brighter than $I_{AB} = 22.5$.

For all galaxies brighter than $I_{AB} = 22.5$, absolute rest-frame magnitudes and stellar masses were obtained using standard multi-color spectral energy distribution (SED) fitting techniques, using the secure spectroscopic redshift, if available, or the photometric one. Stellar masses were obtained using the *hyperzmass* code (Pozzetti et al. 2010; Bolzonella et al. 2010), by assuming a Chabrier initial mass function (Chabrier 2003). To establish mass completeness, Pozzetti et al. (2010) defined a minimum mass (M_{min}) at each redshift above which the derived galaxy stellar mass function is essentially complete (all types of galaxies are potentially observable). To derive M_{min} , the limiting stellar mass (M_{lim}) of each galaxy is calculated, namely the mass the galaxy would have, at its spectroscopic redshift, if its apparent magnitude were equal to the limiting magnitude of the survey. Then, to derive a representative limit for the sample, the authors used the M_{lim} of the 20% faintest galaxies at each redshift. $M_{\text{min}}(z)$ is defined as the upper limit of the M_{lim} distribution below which 95% of the M_{lim} values at each redshift are represented. This is assumed to be the completeness limit of the galaxy stellar mass function.

2.2. Analyzed galaxy sample

To create the bins that collect the galaxies to be stacked, we used the Bright zCOSMOS spectroscopic catalog (v4.12 version). For AGN that are more luminous than the host galaxy, such as the type-1 AGN, whose emission is not screened by the dusty torus (AGN-unification model by Padovani & Urry 1992), we are unable to see the emission lines from the host galaxy. Therefore, we

Table 1. Number of galaxies in each mass-redshift bin of the sample.

M_m/z_m	0.21	0.27	0.34	0.4	0.59	0.67	0.76	0.84
11.12	–	24	83	47	52	133	101	114
10.87	51	42	148	107	106	241	237	189
10.62	63	45	196	118	146	324	296	221
10.37	68	69	177	143	168	323	272	198
10.12	57	66	189	156	187	283	216	173
9.87	52	79	214	152	179	286	219	201
9.62	76	73	213	162	193	238	185	87
9.37	83	95	266	211	–	–	–	–
9.12	108	109	–	–	–	–	–	–

Notes. The table reflects the order of the mass-redshift bins shown in Fig. 1. The median mass (first column) is expressed in $\log M_*/M_\odot$. The median redshift is indicated at the top of each row.

removed type-1 AGN to avoid overshining. This was performed by excluding all objects with broad emission lines. Furthermore, we decided to exclude from our sample all sources without an indication of well-measured spectroscopic redshift. These and the broad-line AGN constitute, all together, about 6% of the original sample within $0.1 < z < 1$ (16 678 objects). In particular, we excluded 892 low-flag objects and 35 broad-line AGN. There are 15 715 galaxies flagged reliable. Another significant fraction of galaxies is lost during the binning process because we excluded underrepresented regions of the redshift-stellar mass diagram (see next section). After applying these selection criteria, we are able to study roughly half of the original zCOSMOS-Bright sample.

3. Spectral analysis

In this section we describe how we exploited the large number of zCOSMOS galaxies by dividing them into various redshift- and mass bins. This was done to obtain average spectra with high S/N and to investigate the evolution of the spectral properties of the stacked galaxies. We aim to study the variation of average properties of galaxies that are representative of a particular mass-redshift bin. After obtaining the spectra, we estimated and subtracted the stellar contribution. Then, we measured line fluxes and computed the visual extinction. Finally, we used diagnostic diagrams to distinguish between the main ionizing mechanism inside these objects. Several programs and tasks were used for this work, most of them running in the image reduction and analysis facility (IRAF) environment.

3.1. Sample binning

To search for variations of galaxy spectral properties as a function of redshift and stellar mass, we divided our large sample into bins. The bin width was tested to achieve a good S/N with the largest number of mass-redshift bins. In particular, we tested the increase in S/N according to the increase in the number of stacked spectra. The first indication of a link between total galaxy stellar mass (M_*) and classification in the spectral types – AGN, composite galaxies, star-forming galaxies – made us opt for a fine grid in M_* . The variations we applied to the size of the redshift intervals did not affect the classification significantly. We afterwards decided for the number of z bins to be equal to 8, with a redshift step ~ 0.1 dex. We divided the sample into nine mass bins, with a mass step of 0.25 dex. The bins include several hundreds of objects for each redshift- and mass range (see Table 1). For our sample selection, mass completeness was

achieved when galaxies above the completeness curves (Pozzetti et al. 2010) were included in the bins. While at lower redshift most bins lie above the completeness limits, at higher redshifts roughly half of the bins are placed below the confidence curves. Although in this case the sample suffers from incompleteness, we chose to study all high-redshift bins to probe a dynamical range of masses comparable with the low-redshift case.

The bins were chosen according to these additional considerations:

- below 9 and above 11.25 $\log M_*/M_\odot$, objects are poorly represented in our sample. The S/N ratio of the average spectra made out of the stacking of an insufficient number of galaxies would not allow precise line measurements;
- eight bins (four per region covered by each of the two types of diagnostic diagrams, $z \lesssim 0.5$ for the low-redshift diagnostic diagrams and $z \gtrsim 0.5$ for the high-redshift diagnostic diagram) are a good compromise between the need to explore the cosmological evolution of the galaxy spectral properties and to keep the number of objects per bin (hence the S/N) high enough.

For diagnostic diagrams based on [NII], [SII], $H\alpha$, [OIII] and $H\beta$, the affected rest-frame spectral range is 4800 to 6650 Å. The zCOSMOS spectra cover the 5650 to 9550 Å range after cutting off 100 Å at both extremes to avoid noisy regions where the flux calibration is more uncertain. The useful redshift range for the low-redshift diagnostic diagrams is then $0.177 \leq z \leq 0.436$. In the same way, the redshift range for the high-redshift diagnostic diagram is $0.548 \leq z \leq 0.884$.

In Fig. 1 we plot the zCOSMOS galaxies as a function of the total galaxy stellar mass. The plot displays our bin selection and the large-scale structure within the zCOSMOS field. The general trend is a clear increase of the average stellar mass with the redshift due to the well-known selection effects of a magnitude-limited survey, with overdense regions (filaments), e.g., at $0.3 \gtrsim z \gtrsim 0.4$ or $0.7 \gtrsim z \gtrsim 0.8$, and underdense regions (voids), e.g., at $z \sim 0.25$. At low redshift the minimum mass (M_{\min}) of the global galaxy population is better represented by the blue population, while it is closer to the red population if we are at higher redshift. This is because blue galaxies dominate the mass function at low redshift, because of selection effects. On the other hand, at high redshift the global M_{\min} shifts toward the limit of the reddest population, since the galaxies have a higher mass-to-light ratio (M/L) on average.

3.2. Stacking

After the binning process, the spectra were stacked. Since each stacked spectra is the result of the average of up to several hundreds of single galaxy spectra included in a single bin, the gain in S/N is considerable and allows a more accurate line fitting. To create the composites, each spectrum was shifted to the rest-frame. The spectra were normalized in wavelength ranges always present in the observed spectroscopic window and lacking prominent spectral features. The wavelengths of the chosen ranges are 5300–5800 Å for $0.177 < z < 0.371$; 4500–4800 Å for $0.371 < z < 0.716$; and 3400–3700 Å for $0.716 < z < 0.884$. Stacked spectra are shown in Appendix A. The main emission- and absorption-lines are labeled at the top of each figure.

The stacked zCOSMOS spectra present, especially for the objects with low masses, a quite blue and featureless continuum at low redshift. The spectra are characterized by strong low-ionization emission lines such as [NII], [SII] and, [OIII]

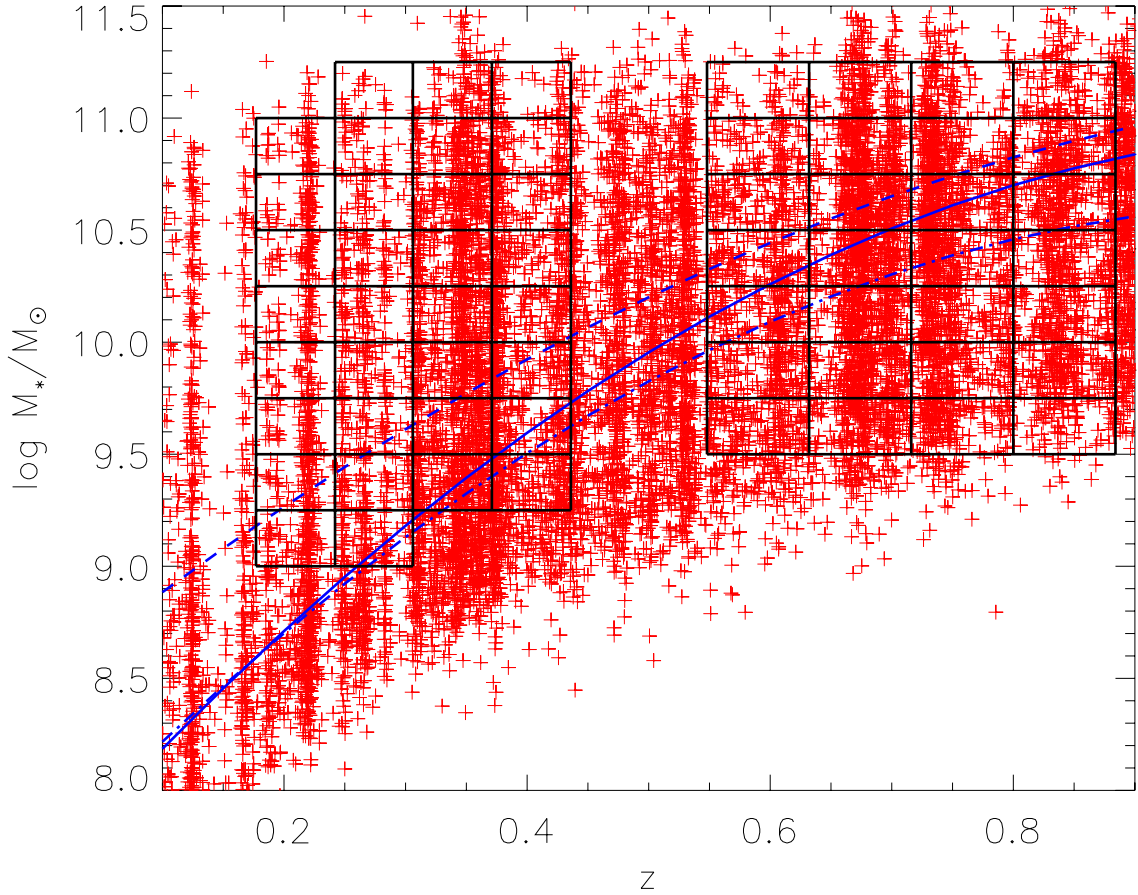


Fig. 1. Stellar mass of zCOSMOS 20k galaxies selected for our study (secure flags, no broad-line AGN) plotted as a function of redshift. The blue dashed lines represent the mass completeness limits of the global galaxy population (solid), the population of early-type (dashed) and the late-type galaxies (dot-dashed). The black boxes mark the 61 mass-redshift bins that define the stacked galaxies we studied with the diagnostic diagrams.

and strong recombination lines of the Balmer series, as expected from the spectral contribution of a young stellar population. On the other hand, the continuum is much redder and displays a strong D4000 break at higher redshift, which is indicative of an older stellar population. The spectra show that the most massive galaxies are spectroscopically more evolved at a given redshift, according to the downsizing scenario.

3.3. Stellar continuum subtraction

Galaxy emission lines – in particular those from the Balmer series – are often contaminated by absorption lines produced by the atmospheres of fairly massive stars within the galaxies. Since our spectra are characterized by both emission from the hot ionized gas and absorption from the stellar component, we need an effective strategy to precisely measure spectral features involved in the diagnostic diagrams. The technique we adopted to remove the starlight from an integrated spectrum was to subtract a suitable model of stellar continuum from each stacked galaxy spectrum to obtain an almost pure emission-line spectrum. This is particularly helpful in correcting the strength of Balmer lines, which are involved in both the AGN identification and the computation of the visual extinction. The procedure also aims to gain additional information on stellar populations, such as age and metallicity, which would have been lost if we had focused on emission lines only. For this purpose, we developed a user-written IRAF task that performs the spectra continuum subtraction. The spectral library to be fitted to the stacked spectra

must contain enough information on various absorption features, to be able to simulate the stellar components of galaxies within a wide range of ages and metallicities. We adopted the Bruzual and Charlot (BC) library, which is a library of stellar population synthesis models computed by Bruzual and Charlot using their isochrone synthesis spectral evolutionary code (Bruzual & Charlot 2003, hereafter BC03). This code allows one to predict the spectral evolution of stellar populations in various ranges of ages and metallicities at a resolution of 3 Å across the whole wavelength range (from 3200 Å to 9500 Å). Models with different time scales of star formation, initial mass functions, and metallicities reproduce the spectral and photometric properties of nearby galaxies with various morphological types well, from young irregulars to elliptical galaxies. For each BC template, we created five spectra with increasing $B(E-V)$ values (0.2, 0.4, 0.6, 0.8 and 1) to take reddening due to dust into account. A total of 234 stellar templates were compared with the stacked spectra to find the one most suitable to be subtracted from each composite. The continuum subtraction task degrades the resolution of the template spectra to that of zCOSMOS ($R \sim 600$). Then, the template was chosen to have the lowest residuals in pre-selected regions of the continuum-subtracted sample that were free from strong emission lines. These spectral windows have a typical width of ~ 100 Å. They span a range between 3600 and 7300 Å for an overall coverage of about 2300 Å.

The stellar continuum subtraction procedure successfully corrects for the underlying stellar absorption (Figs. 2, 3). This feature is particularly noticeable in the highest redshift bins

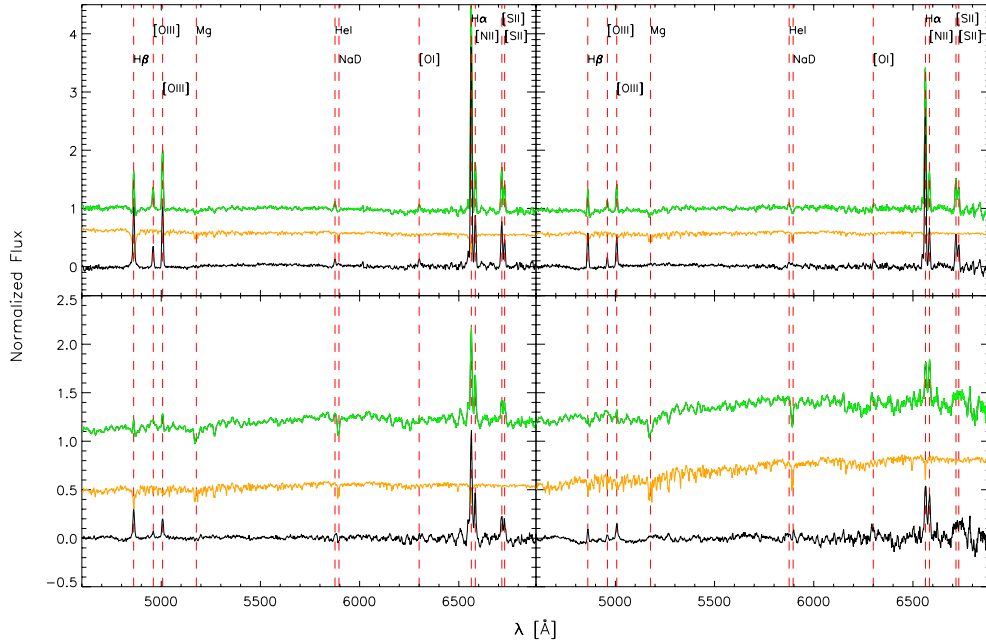


Fig. 2. Four examples of stellar continuum subtraction at low redshift ($z < 0.436$, one per redshift bin). For each panel, the original stacked spectrum (green), the most suitable stellar continuum to be subtracted (orange) and the resulting zCOSMOS stacked spectrum after the stellar continuum subtraction (black) are shown. The main emission and absorption lines are labeled at the top. From *top to bottom* and from *left to right* total stellar mass and redshift increase. *Top-left panel:* stacked spectrum of the bin $9.25 \leq \log M_*/M_\odot < 9.5$, $0.177 \leq z < 0.242$, stellar template representing a 290-Myr-old simple stellar population (SSP) with $Z = 0.2$ and $E(B - V) = 0.4$; *top-right panel:* $9.75 < \log M_*/M_\odot \leq 10$, $0.242 \leq z < 0.306$, 12-Gyr-old stellar template with exponential decay of the star formation, $Z = 0.2$ and $E(B - V) = 0.2$; *bottom-left panel:* $10.25 \leq \log M_*/M_\odot < 10.5$, $0.306 \leq z < 0.371$, 900-Myr-old SSP with $Z = 0.5$ and $E(B - V) = 0.4$; *bottom-right panel:* $10.75 \leq \log M_*/M_\odot < 11$, $0.371 \leq z < 0.436$, 11-Gyr-old SSP with $Z = 0.2$ and $E(B - V) = 0.4$. The stacked spectra before stellar continuum subtraction and the stellar templates have been shifted up by arbitrary quantities for clarity.

(Fig. 3), where the strong stellar contribution to the galaxies spectra comes from older stellar populations.

3.4. Emission line measurement

We measured the flux of [OII], $H\gamma$ 4340 (hereafter $H\gamma$), $H\beta$, [OIII], $H\alpha$, [NII] and [SII]. We used the Splot interactive IRAF task to make spectral measurements of Gaussian-like emission lines. $H\alpha$ and $H\beta$, along with the oxygen lines, [NII] and [SII], were used to exploit the diagnostic diagrams. The measurement errors of the emission lines in our stacked spectra corrected for the stellar absorption are typically lower than 20%, estimated on the basis of repeated independent measurements. The errors mainly depend on the line intensity and whether the emission line is blended with other spectral features. The resolution of the zCOSMOS spectra is sufficient to resolve the [SII] doublet in most of the composites, but it is not sufficient to resolve the [OII] doublet, which always appears as a blended feature.

For the highest stellar masses, the emission line measurements are more difficult because the S/N ratio is lower due to poorer statistics, moreover the lines become weaker and the continuum stronger, especially at high redshift.

3.5. Reddening correction

Observed fluxes need to be corrected for extinction. The total visual extinction, A_V , can be determined by using the ratio between two recombination lines of the Balmer series. For this purpose, $H\alpha$ and $H\beta$ are commonly preferred because they are strong lines placed in an easily accessible spectroscopic position. In this work, we assumed the $H\alpha/H\beta$ theoretical ratio to be 2.86 and the

$H\gamma/H\delta$ to be 0.47 (Osterbrock 1989, case B recombination, temperature $T = 10^4$ K, electron density $n_e = 10^2 \text{ cm}^{-2}$), and we assumed the Calzetti extinction curve (Calzetti et al. 1994) with $R_V = 4.05 \pm 0.8$.

In diagnostic diagrams that use lines that are close to each other in the spectrum, their ratio is relatively insensitive to reddening effects. Nevertheless, we chose to correct for the visual extinction because the [OII] and $H\beta$ lines are quite far away from each other in wavelength, hence their ratio is sensitive to reddening.

4. Diagnostic diagrams

We adopted the following emission-line diagnostic diagrams:

- [NII]/ $H\alpha$ versus [OIII]/ $H\beta$ ($z < 0.436$) (Baldwin et al. 1981; Veilleux & Osterbrock 1987; Kewley et al. 2001, 2006; Kauffmann et al. 2003)
- [OII]/ $H\beta$ versus [OIII]/ $H\beta$ ($z > 0.548$) (Tresse et al. 1996; Rola et al. 1997; Lamareille et al. 2004; Lamareille 2010)
- MEx diagram (Juneau et al. 2011)

The redshift range $0.436 < z < 0.548$ was excluded from our study because [NII] and $H\alpha$ are redshifted outside the optical spectra and [OII] is not yet visible in the blue part of the spectral range. Therefore, it is not possible to use the first two diagnostic diagrams. We decided to keep the same grid of stellar mass and redshift bins for the MEx diagram. Although it would be technically possible to include the missing redshift range when using the MEx diagram, we expect that this would not change our finding that the AGN classification is more dependent on the stellar mass than on the redshift.

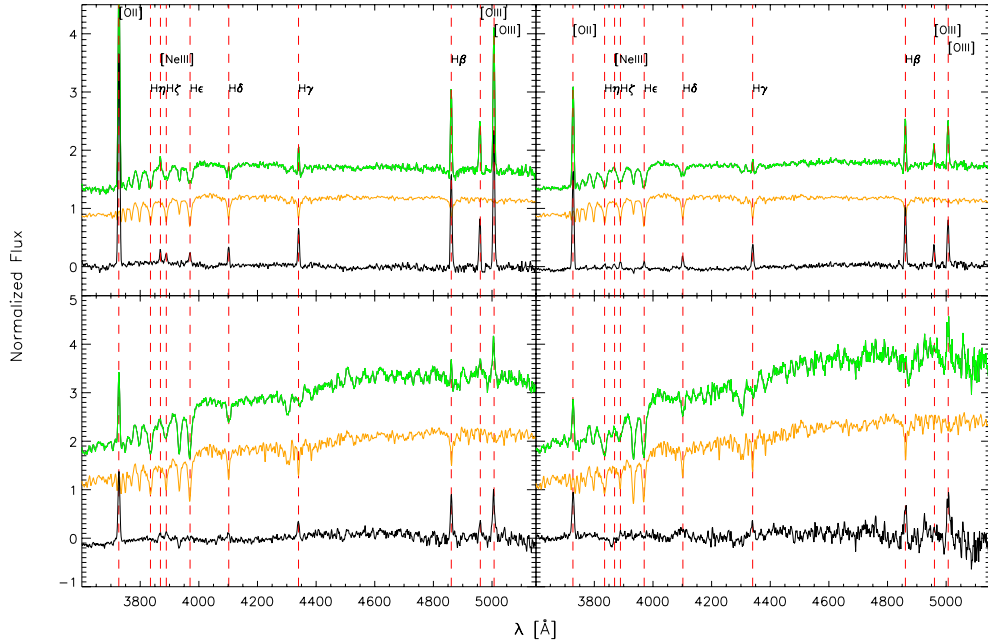


Fig. 3. As in Fig. 2, but at higher redshift ($z > 0.548$). *Top-left panel:* stacked spectrum of the bin $10.5 \leq \log M_*/M_\odot < 10.75$, $0.548 \leq z < 0.632$, stellar template representing a 1.4-Gyr-old SSP with $Z = 0.08$ and $E(B - V) = 0.2$; *top-right panel:* $10.75 < \log M_*/M_\odot \leq 11$, $0.632 \leq z < 0.716$, 1.4-Gyr-old SSP with $Z = 0.2$ and $E(B - V) = 0.2$; *bottom-left panel:* $10.75 \leq \log M_*/M_\odot < 11$, $0.716 \leq z < 0.8$, 1.4-Gyr-old SSP with $Z = 0.08$ and $E(B - V) = 0.2$; *bottom-right panel:* $11 \leq \log M_*/M_\odot < 11.25$, $0.8 \leq z < 0.884$, 1.4-Gyr-old SSP with $Z = 0.2$ and $E(B - V) = 0.2$. The stacked spectra before stellar continuum subtraction and the stellar templates have been shifted up by arbitrary quantities for clarity.

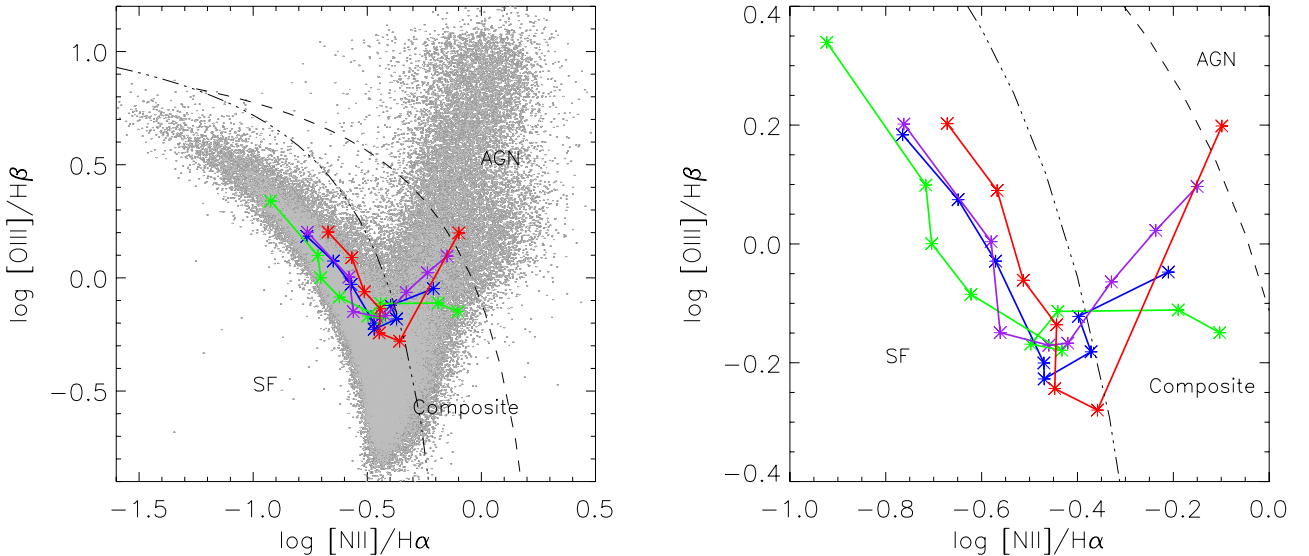


Fig. 4. Classical [NII] diagnostic diagram. A theoretical demarcation curve (dashed, Kewley et al. 2001) separates star-forming galaxies and composites from AGN in the two panels, while an empirical demarcation curve (three-dot-dashed, Kauffmann et al. 2003) separates pure SFGs from composites and AGN. Each color represents the trend with stellar mass for a fixed redshift bin: $0.177 < z < 0.242$ (blue), $0.242 < z < 0.306$ (green), $0.306 < z < 0.371$ (purple), and $0.371 < z < 0.436$ (red). The total stellar mass increases from *left to right*. In the *left panel*, the SDSS galaxies from Vitale et al. (2012) are plotted in gray. The *right panel* offers a closer view of the zCOSMOS galaxies.

4.1. Low-redshift diagnostic diagrams ($0.177 < z < 0.436$)

In the [NII]/H α versus [OIII]/H β or Baldwin-Phillips-Terlevich (BPT) diagram (Baldwin et al. 1981), galaxies are distributed in two arms. The increase of the [NII]/H α ratio is a linear function of the nebular metallicity and presents a saturation point (Denicol et al. 2002; Kewley & Dopita 2002; Pettini & Pagel 2004) above which any additional increase in the [NII]/H α value is only due to AGN contribution (Kewley et al. 2006; Stasińska et al. 2006). The BPT emission-line diagnostic diagram makes

use of different demarcation curves, both theoretical and based on observations. The first curve was derived theoretically by Kewley et al. (2001) to find an upper limit for star-forming galaxies (Fig. 4). Kauffmann et al. (2003), using the large sample of emission line galaxies in the SDSS, defined a demarcation that traces the observed lower left branch more closely, which is attributed to purely star-forming galaxies. This results in a larger portion of galaxies residing on the AGN side (Fig. 4). According to this classification, some of the AGN and composite galaxies with widely spread distributions of metallicity and

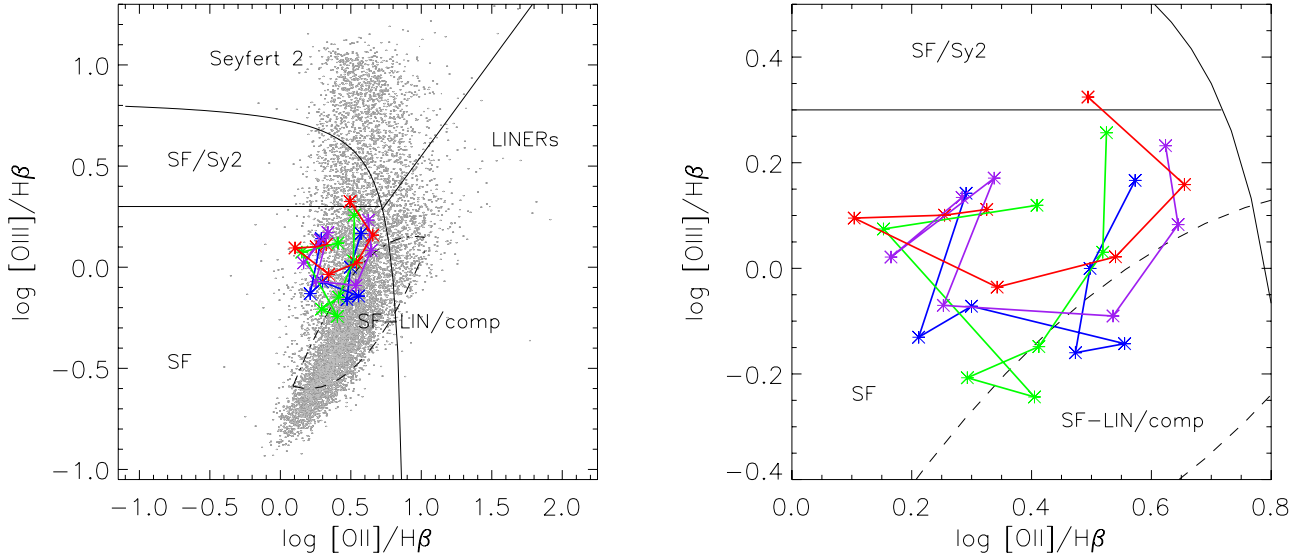


Fig. 5. [OII] diagnostic diagram. [OII]/H β flux dust-corrected ratios are used. The demarcation lines are taken from Lamareille (2010). Each color represents the trend with stellar mass for a fixed redshift bin: $0.548 < z < 0.632$ (blue), $0.632 < z < 0.716$ (green), $0.716 < z < 0.8$ (purple), and $0.8 < z < 0.884$ (red). The total stellar mass increases from left to right. In the left panel, the SDSS galaxies from Vitale et al. (2012) are plotted in gray. The right panel shows a closer view of the zCOSMOS galaxies.

ionization parameters are degenerate with star-forming galaxies. This is especially the case, for example, of the [SII]/H α versus [OIII]/H β diagram.

Objects that are classified as AGN in the [NII]-based diagram can be classified as star-forming galaxies in the [SII]/H α versus [OIII]/H β diagram. This is thought to be related to the enhancement of [SII] lines in starburst galaxies, due to the mechanical energy released into the gas by supernovae and stellar winds (also called shock excitation, Dopita et al. 2002). However, it is still not clear whether the [SII] enhancement is driven by highly ionizing photons produced by accretion onto the super massive BH or if the SNe winds are a sufficiently powerful source of ionization. The [SII]-based diagnostic diagram, due to the fringing and line blending, is more affected by errors and leads to a higher probability of misclassifying galaxies than the [NII]-based diagram. For these reasons, the diagnostic diagram that makes use of the [SII] doublet was not used to draw conclusions but is only shown below as a comparison.

In Fig. 4 (left panel), we show the zCOSMOS data superimposed on the SDSS data from Vitale et al. (2012). Each color represents a different redshift bin and each point along the curve represents a different mass bin. The right panel offers a zoom on the region of the diagram where our data are placed. The stacked spectra show a progressive shift toward the AGN region – on the right-hand side of the diagram – for increasing stellar mass (from left to right). The objects with the highest mass are placed on the right of the Kauffmann demarcation curve, which separates the region where galaxies start to show significant nuclear activity. The stacks follow, for a fixed redshift bin, tracks that move from the upper part of the SF galaxies sequence to the metallicity sequence (Kewley et al. 2006). For $\log M_*/M_\odot > 10.2$, the objects start being classified as composites or AGN, in agreement with what was suggested by Kauffmann et al. (2003) for $z < 0.1$.

4.2. High-redshift diagnostic diagram ($0.548 < z < 0.884$)

For the objects placed at higher redshifts, for which we lack useful AGN-activity indicators such as the [NII], [SII] or [OI] lines, a different kind of diagnostic diagram is needed to determine

the galaxy spectral type. The Lamareille et al. (2004) diagnostics involves the [OII] line (Fig. 5) and represents a high-redshift option to the more classic diagnostic diagrams. Unfortunately, this diagram is strongly biased against composites (Lamareille 2010), which overlap with star-forming galaxies and low ionization nuclear emission regions (LINERs, Heckman 1980). The [OII] emission line is thought to be either an indicator of ongoing star formation or AGN activity, because of the relatively low ionization potential that is required compared with the [NII] or [SII] transitions. As a consequence, this diagnostic diagram cannot be considered as reliable as the set of low-redshift diagnostic diagrams (Bongiorno et al. 2010; Juneau et al. 2011).

In this diagram it becomes necessary to correct line ratios for reddening. This is because the emission-lines that are used as indicators are placed far away from each other in the spectra and therefore are differently affected by reddening. Another way to overcome this problem is to use the equivalent width (EW) of the emission lines. Using the EW instead of the extinction-corrected fluxes does not change our galaxy classification significantly (see Appendix B).

To separate AGN from star-forming galaxies (Fig. 5), we used lines that have been empirically defined by Lamareille (2010) by using galaxies from the SDSS. The left panel of Fig. 5 shows the distribution of SDSS galaxies (in gray) and the zCOSMOS galaxies superimposed on it. For every redshift bin (indicated with different colors) a higher mass means, in most of the cases, a shift toward higher values of [OII]/H β . Although the stacked galaxies show, as in the [NII] diagram (Fig. 4), a trend with the total stellar mass, almost all objects are placed in the SF zone. For the higher masses, we notice that some of the stacked galaxies fall in the region of mixed contribution from star-forming galaxies and LINERs, while only the points representing the highest mass-redshift bin falls in the star-forming/Seyfert region. This poor ability to properly classify AGN using the [OII]/H β ratios was also noticed in the analysis of zCOSMOS spectra for 24 micron-selected galaxies (Caputi et al. 2008, 2009). The diagram is known to be the most sensitive to shocks. This might be the reason why some objects are likely to be misclassified as star-forming galaxies rather than LINERs,

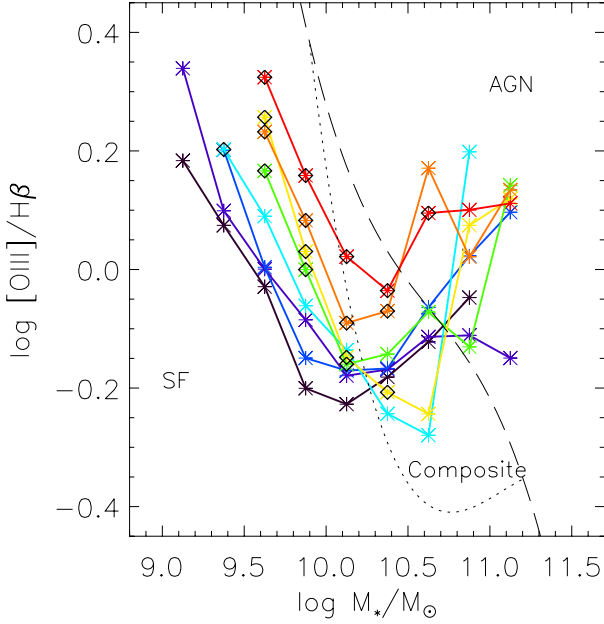


Fig. 6. New diagnostic diagram (MEx) by Juneau et al. (2011) uses the stellar mass instead of the $[\text{NII}]/\text{H}\alpha$ emission line ratio. In this plot, every color represents the evolution in mass for a fixed redshift bin (the whole z -range): $0.177 < z < 0.242$ (black), $0.242 < z < 0.306$ (purple), $0.306 < z < 0.371$ (blue), $0.371 < z < 0.436$ (light blue), $0.548 < z < 0.632$ (green), $0.632 < z < 0.716$ (yellow), $0.716 < z < 0.8$ (orange), and $0.8 < z < 0.884$ (red). The mass increases from left to right along each track. The black diamonds indicate mass incompleteness (see Fig. 1).

which would appear in a similar position along the y -axis, but at higher $[\text{OII}]/\text{H}\beta$ values.

4.3. New generation of diagnostic diagrams

Classical diagnostic diagrams are largely used by the scientific community to classify AGN from emission line ratios, especially in the optical range. Nevertheless, these diagrams present some problems that make it preferable to look for new and more effective diagnostic methods. Recently, Juneau et al. (2011) adopted a new diagram (MEx diagram) that can be used at higher redshift than the classical diagnostic diagrams. A correlation between galaxy stellar mass and metal content has been observed (mass-metallicity relation, Tremonti et al. 2004; Savaglio et al. 2005) and the $[\text{NII}]/\text{H}\alpha$ ratio is known to trace metallicity for SFGs (Kewley et al. 2006; Stasińska et al. 2006). For this reasons, the authors chose to substitute the emission line ratio $[\text{NII}]/\text{H}\alpha$ in the BPT diagram with the total stellar mass. This new kind of diagnostics has the considerable advantage that one can classify all objects of a quite wide redshift range within a unique diagram. Moreover, it avoids some of the problems connected to the reliability of the $[\text{OII}]$ diagram, though the MEx diagram suffers from more blending between LINERs and Seyfert 2s than the latter.

The mass trend we already observed in the $[\text{NII}]$ diagram is now clear in the MEx diagram (Fig. 6), where we can represent galaxies spanning our entire redshift range. As in Figs. 4 and 5, each color represents a different redshift bin and the points indicate the mass bins. At $\log M_*/M_\odot > 10.2$, the galaxies leave the SF region to enter the composite region of the diagram. With increasing mass, the $[\text{OIII}]/\text{H}\beta$ ratio decreases up to the point where the galaxies start to be classified as composites. Then,

the ratio increases again, as already noted in the $[\text{NII}]$ diagram. While the stellar mass tracks overlap in Figs. 4 and 5, they are parallel to each other in the SF region of the MEx diagram and systematically offset toward the AGN region for increasing redshift (Fig. 6). Therefore, the higher the redshift the higher the number of composites that are classified as transitional objects or AGN. In this respect, the MEx diagram shows the clearest sign of redshift evolution.

5. Discussion

In this section, we discuss our main results and explore future possibilities.

5.1. Average and median stacking

Stacking analyses may be challenging to interpret if the stacked galaxies span a broad range of physical properties. When taking averages, galaxies with strong lines might dominate the signal over objects with intrinsically weaker lines. As an example, we would expect massive galaxies that are star-forming and LINERs to have much weaker lines (in particular $[\text{OIII}]$) compared with Seyferts with the same stellar mass. Therefore, a potential risk would be that a few percent of Seyferts dominate the signal and raise $[\text{OIII}]$ on the stacked spectrum, yielding a biased view that the stacked galaxies are AGN-dominated by number. To search for this effect, we compared the results with median stacking and average stacking. We compared a subsample of two median stacked redshift bins (15 stacks in total). The line ratios we calculated from the stacks obtained with median and average stacking are very similar and lead to the same spectroscopic classification. Therefore, we found no indication of a bias toward more powerful AGN dominating the signal of the stacks. We conclude that there is no substantial difference between median and average stacking of galaxies in our mass-redshift bins. All measurements shown in this paper are from average stacked spectra. We can identify two possible reasons for the similarity between the measurements: a) From the definition of average and median stacking, we expect the difference between the two to be noticeable only when the number of AGN in a particular mass- z bin is very low (compared with the number of star-forming galaxies). From our results and as already expected from previous studies, this is more likely to happen at low masses. However, the chance of noticing a difference between median and average stacking is reduced for a symmetric shape of the underlying distribution (e.g. Gaussian), when in a large sample the median value of the distribution tends to the average value. We dealt with hundreds of galaxies per bin, thus with a statistics that might be large enough to hide this effect. b) The effect is still there, but it is not possible to notice the difference between median and average stacking and the trend is somehow lost in the measurement errors, which we estimate to be $<20\%$ (see Sect. 3.4). In the $[\text{NII}]$ diagram, the typical difference we find on the emission-line ratios is $<5\%$, and $\sim 20\%$ for the $[\text{NII}]/\text{H}\alpha$ and $[\text{OIII}]/\text{H}\beta$ ratios, respectively. In the $[\text{OII}]$ diagram, the difference is $\sim 10\%$ and $\sim 40\%$ for the $[\text{OII}]/\text{H}\beta$ and $[\text{OIII}]/\text{H}\beta$ ratios.

However, we should keep in mind that in our study all low-redshift mass-redshift bins and several of the high-redshift bins are considered to be complete (see Sects. 2.1, 3.1). Hence, each stack is representative of the average behavior of a particular bin.

5.2. Visual extinction

It is known that dust extinction in star-forming galaxies depends upon star-formation rate, metallicity, and stellar mass

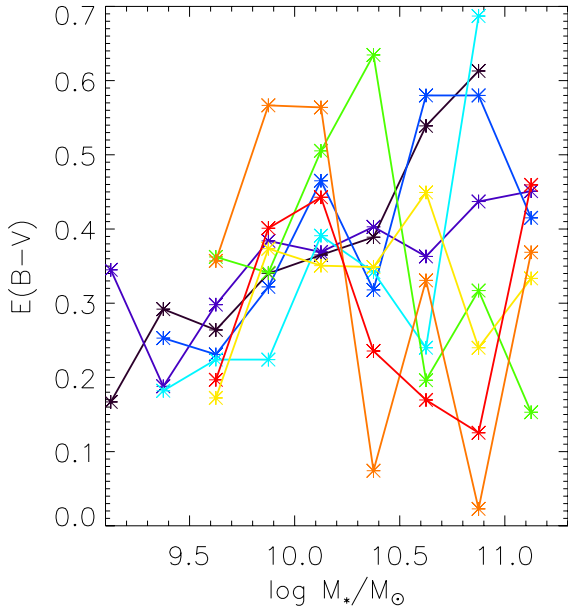


Fig. 7. Measured $E(B - V)$ (inferred from the Balmer ratios) as a function of stellar mass, with tracks corresponding to a given redshift: $0.177 < z < 0.242$ (black), $0.242 < z < 0.306$ (purple), $0.306 < z < 0.371$ (blue), $0.371 < z < 0.436$ (light blue), $0.436 < z < 0.548$ (green), $0.548 < z < 0.632$ (yellow), $0.632 < z < 0.716$ (orange), and $0.716 < z < 0.884$ (red) (see Fig. 1).

(Garn & Best 2010). High extinction values are associated with an increase of any of these three parameters, although the fundamental property connected with extinction seems to be the stellar mass. However, we considered galaxies of different spectral type. We would expect to find increasing values of the visual extinction for higher masses, since the high-mass tail of the galaxy mass function of galaxies placed at high redshift ($z \sim 2$) is populated by ultra luminous infrared galaxies (ULIRGs, infrared luminosity at 8–1000 microns higher than $10^{12} L_{\odot}$, Daddi et al. 2005) that store a large amount of dust that reddens the outgoing light. On the other hand, we may expect the opposite trend, namely a decreasing value of the visual extinction with stellar mass, since on the high tail of the galaxy mass distribution we observe objects that might have experienced AGN feedback (e.g., jets blowing up the gas and dust content). In general, massive systems that have experienced star formation in the past are found to contain only a small amount of gas and dust. Less massive galaxies, according to the downsizing scenario, are more likely in the evolutionary stage where they still have material to fuel the star formation.

We found that the distribution of the $E(B - V)$ values is nearly flat for increasing mass and redshift. In particular, the visual extinction measured from the stellar-continuum-subtracted spectra shows an increment with the stellar mass only in the low-redshift bins (Fig. 7 and Table 2). At higher redshifts the same trend may be hidden by the bigger errors in the measurement of $E(B - V)$ (see Sect. 3.4). On the other hand, the $E(B - V)$ values inferred from the SED fitting results displayed in Table 2 show a different tentative trend. The $E(B - V)$ values are higher in the high-redshift bins, but with no distinction between high and low masses. This evidence is insufficient to indicate what the main contribution to extinction could be – reddening from dusty ULIRGs or low extinction due to AGN feedback. The results seems to weakly suggest a higher extinction for the more massive galaxies, especially if placed at higher redshift. However, more studies are needed to shed light on this topic.

5.3. Diagnostic diagrams

Emission lines are a good indicator of star-forming or AGN activity. By means of diagnostic diagrams and spectral stacking, we found an indication for a link between the total stellar mass and the chance of identifying galaxies as AGN. A temporal evolution – namely, an observed trend with redshift – is also possible but, even if present, it is obscured within the classical diagnostic diagrams. This could be because our redshift bins are too close to each other for the stacked galaxies to show a trend with redshift in the classification provided by the diagrams. It is important to notice that we are studying a cosmic period ($z < 1$) that is considered as crucial for AGN feedback and quenching of the star formation to happen, because it has seen both the drop in star formation history and the build-up of about half of the red sequence (Bell et al. 2007; Faber et al. 2007). However, the time interval over which to probe evolutionary effects is longer when using the MEx diagram ($0.17 \lesssim z \lesssim 0.88$) than when using the BPT ($0.17 \lesssim z \lesssim 0.44$) or [OII]-based ($0.55 \lesssim z \lesssim 0.88$) diagrams alone.

The indication of an evolutionary trend is present in the MEx diagram (Fig. 6). Here the data points representing galaxies in the same mass range are progressively offset to higher values of [OIII]/H β for increasing redshift. On the other hand, along each track (fixed redshift, increasing stellar mass) the data show a metal enhancement (see also Fig. 4). The reason for the latter could be researched in the mass-metallicity relation and the efficiency of galactic winds in removing metals from low-mass galaxies (Lequeux et al. 1979; Tremonti et al. 2004; Maiolino et al. 2008). Outflows generated by starburst winds may easily eject metal-enriched gas from low-mass galaxies placed at low redshifts, making their enrichment less significant than in massive systems (Tremonti et al. 2004). Moreover, low-mass systems are, according to the galaxy-downsizing scenario (Juneau et al. 2005; Asari et al. 2007; Pérez-González et al. 2008), at an earlier evolutionary stage, where they are still converting most of their gas into stars. For this reason they are poorly metal-enriched compared with massive galaxies. However, it should be kept in mind that our purely magnitude-limited sample suffers from selection biases and mass incompleteness toward the highest redshifts, where most of the AGN are found among the stacked galaxies. The set of classical diagnostic diagrams turned out to be not completely suitable for our study. While the [NII] diagram nicely shows that the mass can determine the galaxy classification, the [SII] – due to the problems already discussed in Sect. 4.1 – does not show the same trend and classifies all stacked galaxies as SF (Fig. 8). The [OII]-based diagram, on the other hand, leaves us with big uncertainties because of the intrinsic nature of the diagram itself (rather sensitive to shocks, it is unable to distinguish the contribution of stellar sources from AGN). Indeed, the diagram shows an overlap between star-forming galaxies and Seyfert 2s, as well as an overlap between the former and composites. However, the higher-mass galaxies are closer to the demarcation line and the AGN region. Using the MEx diagnostic diagram partially solves the problems related to the ineffectiveness of the classical diagnostic diagram at high redshift ([OIII]) and enables one to look for AGN contamination at high masses (see next section). The mass threshold above which the objects start to be classified as composite and AGN is well visible.

5.4. Quenching of the star formation

We noticed a general increase of the age of the stellar populations for increasing mass at both high and low redshifts. Table 2

Table 2. Information on the stacked galaxies of the mass-redshift bin of Fig. 1.

SSP 1.4 Gyr AGN	0.2	SSP 2.5 Gyr AGN	0.2	SSP 1.4 Gyr AGN	0.2	SSP 1.4 Gyr AGN	0.2	SSP 2.5 Gyr AGN	0.2	SSP 1.4 Gyr AGN	0.2	SSP 2.5 Gyr AGN	0.2	SSP 1.4 Gyr AGN	0.2	SSP 1.4 Gyr AGN	0.2
0.613	0.5	0.437	0.2	0.580	0.2	0.415	0.5	0.011	0.5	0.011	0.5	0.153	0.08	0.369	0.5	0.459	0.2
SSP 2.5 Gyr Comp	0.2	SSP 1.4 Gyr Comp	0.2	SSP 2.5 Gyr Comp	0.2	SSP 1.4 Gyr Comp	0.2	SSP 1.4 Gyr Comp	0.2	SSP 1.4 Gyr Comp	0.2	SSP 1.4 Gyr Comp	0.2	SSP 1.4 Gyr Comp	0.2	SSP 1.4 Gyr Comp	0.2
0.539	0.08	0.363	0.2	0.580	0.2	0.580	0.2	0.687	0.2	0.687	0.2	0.317	0.2	0.023	0.08	0.125	0.08
Exp 12 Gyr SF	0.2	SSP 1.4 Gyr Comp	0.2	SSP 2.5 Gyr Comp	0.2	SSP 1.4 Gyr Comp	0.2	SSP 1.4 Gyr Comp	0.2	SSP 1.4 Gyr Comp	0.2	SSP 1.4 Gyr Comp	0.2	SSP 1.4 Gyr Comp	0.2	SSP 1.4 Gyr Comp	0.2
0.389	0.2	0.403	0.2	0.318	0.5	0.342	0.5	0.342	0.5	0.342	0.5	0.196	0.08	0.331	0.08	0.170	0.5
SSP 900 Myr SF	0.2	SSP 900 Myr SF	0.2	SSP 1.4 Gyr SF	0.2	SSP 1.4 Gyr SF	0.2	SSP 1.4 Gyr SF	0.2	SSP 1.4 Gyr SF	0.2	SSP 1.4 Gyr SF	0.2	SSP 1.4 Gyr SF	0.2	SSP 1.4 Gyr SF	0.2
0.365	0.5	0.369	0.2	0.465	0.08	0.391	0.08	0.391	0.08	0.391	0.08	0.505	0.08	0.563	0.08	0.443	0.2
Exp 12 Gyr SF	0.2	SSP 640 Myr SF	0.2	SSP 640 Myr SF	0.2	SSP 1.4 Gyr SF	0.2	SSP 1.4 Gyr SF	0.2	SSP 1.4 Gyr SF	0.2	SSP 1.4 Gyr SF	0.2	SSP 1.4 Gyr SF	0.2	SSP 1.4 Gyr SF	0.2
0.340	0.2	0.384	0.2	0.322	0.5	0.244	0.2	0.244	0.2	0.244	0.2	0.341	0.08	0.567	0.2	0.401	0.08
SSP 640 Myr SF	0.2	SSP 640 Myr SF	0.2	SSP 900 Myr SF	0.2	SSP 900 Myr SF	0.2	SSP 900 Myr SF	0.2	SSP 900 Myr SF	0.2	SSP 900 Myr SF	0.2	SSP 900 Myr SF	0.2	SSP 900 Myr SF	0.2
0.264	0.5	0.298	0.2	0.231	0.5	0.224	0.08	0.224	0.08	0.224	0.08	0.362	0.08	0.172	0.08	0.197	0.5
SSP 290 Myr SF	0.4	SSP 640 Myr SF	0.2	Exp 12 Gyr SF	0.2	Exp 12 Gyr SF	0.2	Exp 12 Gyr SF	0.2	Exp 12 Gyr SF	0.2	Exp 12 Gyr SF	0.2	Exp 12 Gyr SF	0.2	Exp 12 Gyr SF	0.2
0.292	0.2	0.188	0.2	0.253	0.08	0.182	0.08	0.182	0.08	0.182	0.08	0.362	0.08	0.172	0.08	0.197	0.5
SSP 900 Myr SF	0.2	SSP 1.4 Gyr SF	0.2	SSP 1.4 Gyr SF	0.2	SSP 1.4 Gyr SF	0.2	SSP 1.4 Gyr SF	0.2	SSP 1.4 Gyr SF	0.2	SSP 1.4 Gyr SF	0.2	SSP 1.4 Gyr SF	0.2	SSP 1.4 Gyr SF	0.2
0.167	0.08	0.345	0.08	0.345	0.08	0.345	0.08	0.345	0.08	0.345	0.08	0.345	0.08	0.345	0.08	0.345	0.08

SP	E(B-V) _s
E(B-V) _m	Z

Notes. We provide in each box a template of stellar population that best fits the stacked zCOSMOS spectrum (SP, top-left); reddening of the stellar spectrum ($E(B - V)_s$, top-right); value of the extinction as measured from the Balmer ratios after stellar continuum subtraction ($E(B - V)_m$, bottom-left); metallicity (Z, bottom-right); spectral classification (Class, middle of the box) according to the MEx diagnostic diagram. SSP, CSP, and Exp stand for simple stellar population, constant stellar template, and exponential decay of the star formation. The legend is given at the bottom-right of the table.

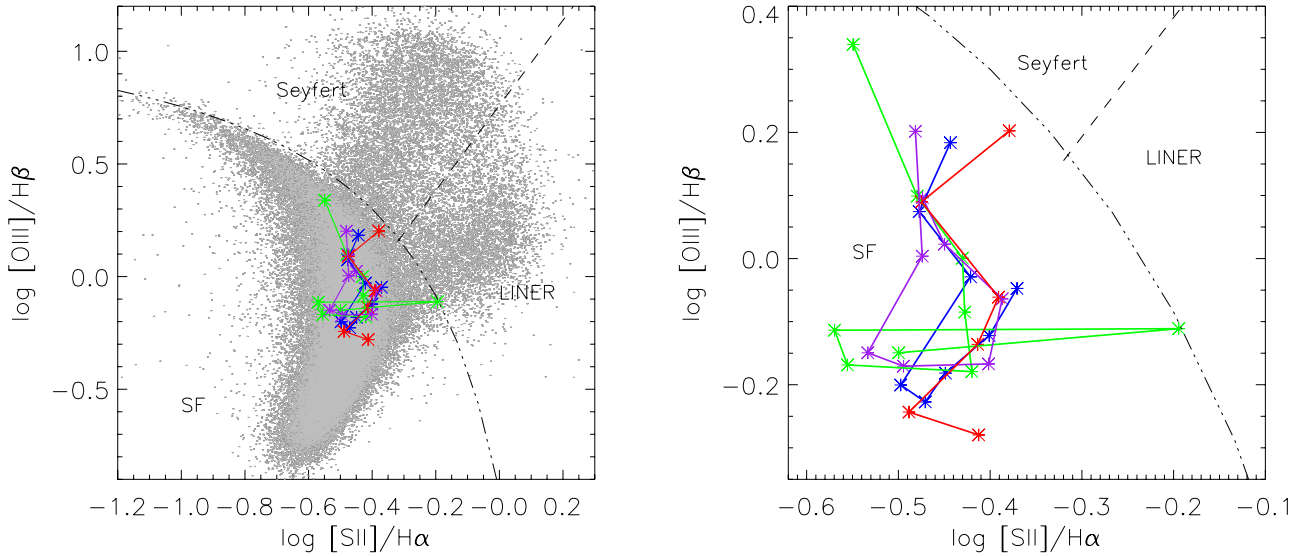


Fig. 8. Classical [SII] diagnostic diagram. In both panels demarcation curves by Kewley et al. (2006) separate star-forming galaxies from Seyferts and LINERs. Each color represents the trend with stellar mass for a fixed redshift bin: $0.177 < z < 0.242$ (blue), $0.242 < z < 0.306$ (green), $0.306 < z < 0.371$ (purple), and $0.371 < z < 0.436$ (red). The total stellar mass increases along each track, starting from the top. In the *left panel*, the SDSS galaxies from Vitale et al. (2012) are plotted in gray. The *right panel* offers a closer view of the zCOSMOS galaxies.

summarizes all information on the stacked galaxy spectra in the stellar mass and redshift bins illustrated in Fig. 1. The most suitable stellar continuum template to be subtracted from each stacked spectrum was chosen from the set of 234 stellar templates (39 BC templates \times 5 reddened spectra). The table shows the reddening inferred from the stellar template, $E(B - V)_s$, and the reddening calculated from the Balmer lines, $E(B - V)_m$, whose fluxes were measured from the stellar-continuum subtracted spectra. The metallicity of the stellar template gives an important indication of the age-metallicity degeneracy (Worthey 1994). For a fixed redshift and along the mass sequence (Fig. 1, Table 2), the stellar populations become progressively older. A young stellar population following an older one in the mass sequence in most cases presents a higher metallicity and a higher reddening than inferred from the stellar fit. A stellar population following one of the same age along the mass sequence is often characterized by equal or higher values of Z and $E(B - V)_s$.

This evidence finds a possible explanation in the mass-assembly downsizing scenario, where most of the massive galaxies build their mass earlier than lower-mass galaxies (Cowie et al. 1996; Kodama et al. 2004; Thomas et al. 2005; Tanaka et al. 2005; Juneau et al. 2005; Bundy et al. 2006). According to this scenario, the number of red massive objects is constant up to $z = 1$, dominating as the main contribution to the mass population, while the number density of red galaxies with $M < 10^{11} M_\odot$ increases with cosmic time. Conversely, the number density of blue galaxies decreases from $z = 1$ to today. Downsizing suggests that something turns the galaxy transformation out at around $z = 1$. If the most massive objects build their mass during an earlier period of time than the less massive galaxies, we expect to find older stellar populations in the former because they had more time to evolve.

If the effect of having younger stellar populations at higher redshifts was already expected from different galaxy evolutionary scenarios, the evidence of older stellar populations with increasing mass and fixed redshift points to the downsizing scenario in particular. It is likely that a mechanism acted to quench the star formation in these objects. Now the question is: can this process be an AGN-feedback? Considering the downsizing

scenario where young low-mass galaxies are still undergoing star formation and high-mass galaxies are the product of an earlier mass assembly, the latter are passively evolving galaxies without star formation episodes. In this respect, AGN might have just suppressed star formation with their feedback by means of transforming blue galaxies into red ones that continue to accrete mass. As a support to this theory, it has been found that the stellar population of the host galaxies appears to be older after the AGN active phase (Sarzi et al. 2005). Currently, several theories and models include AGN feedback, but observational evidence is still needed to prove them right.

5.5. AGN identification

The downsizing scenario takes into account a quenching mechanism to explain galaxy evolution. Our findings fit into the big frame of this latter scenario. Table 2 reports the spectral classification (AGN, composite, or SF) of the stacked zCOSMOS galaxies according to the MEx diagnostic diagram (Fig. 6). Clearly AGNs are common amongst the high-mass bins. This is particularly true for higher redshift bins. However, some stacked spectra are placed directly on the demarcation curves that separate AGN from composites, or immediately next them. In these cases, either the stacking galaxies do not belong to a single population – namely, they are a mixture of AGN and star-forming galaxies – or the underlying population is truly dominated by composite galaxies.

Using stacked spectra instead of individual spectra leads to some difficulties in estimating the number of SFGs and AGN. If, on one hand, this technique allows one to study the average properties of galaxies in a given mass-redshift bin – providing average spectra for otherwise individually unclassifiable galaxies with too low S/N – on the other hand it does not provide us with the exact number of spectral types. Furthermore, each bin collects a variable number of galaxies, because of filaments (overdensities), voids (underdensities), and selection effects acting at the highest as well as at the lowest stellar masses (Fig. 1 and Table 1). Therefore, it is not possible to compare the exact number of AGN between the different bins. Assuming

that all galaxies in a given stack have the same classification as the stacked spectrum, we obtain the following statistics. The number of single galaxies that are spectroscopically identified as AGN in the high-redshift bins (5568 galaxies in total) is 1690 (30.3%), while there are 2491 composites (44.7%). These numbers are higher than the galaxies placed in bins at lower redshift (3742 galaxies), where we find 395 AGN (10.5%) and 775 composites (20.7%). However, assuming that all galaxies in a given composite or AGN bin are indeed AGNs will very likely result in an overestimate of the true AGN fraction. Nevertheless, the relative difference between the higher and lower redshift bins remains an interesting hint of a greater AGN fraction at earlier epoch. Based on the study of individual galaxy spectra, Ivezic et al. (2002) found a starburst-over-AGN ratio equal to 18 from SDSS data, which is a much higher ratio than we found.

The search for AGN could benefit from the complementary analysis of individual galaxy spectra or from analyses at other wavelengths. The X-domain can identify AGN because the luminous, compact X-ray emission ($L_{2-10 \text{ keV}} > 10^{42} \text{ erg s}^{-1}$) is an almost certain indicator that there is an AGN (Bauer et al. 2004; Brandt & Hasinger 2005; Comastri & Brusa 2008; Brandt & Alexander 2010), given the extremely low contribution from star formation to the overall emission at these frequencies. X-ray observations have been found to be very efficient in revealing accreting BHs in galaxies that were not classified as AGN from the analysis of optical data (see Brusa et al. 2010, and references therein). This suggests that the use of multi-wavelength data can be beneficial in AGN-host studies. The *XMM-Newton* wide-field survey in the COSMOS field (Hasinger et al. 2007) provides a large sample of point-like X-ray sources (~ 1800) with complete ultraviolet to mid-infrared (including *Spitzer* data) and radio coverage. The survey – thanks to the high efficiency of X-ray observations in identifying AGN – currently allows further investigations (e.g. Brusa et al. 2010) and contributes to answering questions on galaxy-BH coevolution up to high redshifts.

5.6. Aperture effects

Aperture biases are particularly important in emission-line studies. Spectroscopic observations are performed using different aperture sizes, depending on the specific instrument. This problem plays a critical role in distinguishing the main contribution to galaxy emission. The so-called aperture effect tells us that the shape and size of the instrument aperture influences the galaxy classification. We would expect big fibers/slits to select emission from all over the galaxy, hence several contributions to the line emission (AGN from the nucleus, starburst from the outer regions of the host galaxy) are present. On the other hand, a smaller aperture would mainly select light coming from the nucleus and the bulge, missing the disk where most of the star formation takes place. For example, SDSS data are known to be affected by an aperture effect because of the large fixed size ($3''$) of the fiber used for observations, which includes on average $>20\%$ of galaxies area at $z > 0.04$ (Kewley et al. 2006). Therefore, the stellar contribution to the emission from the host causes a large number of sources to be classified as transitional objects in the diagnostic diagrams. The same argument applies at higher redshift, where the slit width becomes similar to the typical angular size of galaxies. Furthermore, higher-redshift galaxies present higher star formation rates, so the effect of host galaxy dilution of the AGN signatures could be even more important and yield more often composite signatures. From this point of view, with the $1''$ width of the slits used for the zCOSMOS observations and a seeing always better than $1.2''$ (Lilly et al. 2007), our sample is

less sensitive to contamination from emission coming from the most outer regions of the galaxies than other studies at similar redshift.

However, the conventional belief that smaller apertures select more AGN-like emission has been challenged in Shields et al. (2007). The authors showed that for many composite objects identified in the Palomar spectroscopic survey (Ho et al. 1997b) the observed line-ratios do not appear more AGN-like with smaller apertures ($10\text{--}20 \text{ pc}$). Therefore, the aperture effect problem remains controversial and it is worth more studies.

6. Summary and conclusions

We used the zCOSMOS 20k catalog to create a sample of galaxies with reliable spectroscopic redshift and without broad-line AGN to avoid overshining problem (AGN brighter than the surrounding galaxy) and investigated the evolution of galaxy spectral properties up to $z \sim 1$. The sample, containing $\sim 1.5 \times 10^4$ objects, was divided into 61 bins over the stellar mass-redshift plane (Fig. 1). This was done taking into account the completeness in mass and the gap in redshift, this latter because it is impossible to measure all emission lines of the classical diagnostic diagrams. To improve the S/N of the single spectra, we combined all spectra in each bin to obtain stacks, allowing accurate flux measurements. After stacking the spectra, we performed the stellar continuum subtraction on the galaxy composites, using templates of stellar population synthesis. This provided new spectra that are almost free from absorption contaminations by stars, and also gave information on the age of the stellar populations and their composition (metallicity). Finally, we applied optical emission-line diagnostics to search for AGN contamination at the highest stellar masses.

Our main findings are:

- The visual extinction of the galaxies inferred from the Balmer ratios does not show a strong trend with the total stellar mass throughout the z range. It increases slightly at low redshifts for increasing mass, but there is no indication of a clear trend at higher redshifts.
- Galaxy stellar populations are older (in terms of time from the last burst of star formation) for more massive objects. This agrees with an evolutionary scenario that accounts for a fast mass assembling and stellar population aging for massive objects.
- In general, galaxy-stacked spectra are more likely to be classified as AGN than star-forming galaxies for high values of their total stellar mass. In particular, we found that galaxies with $\log M_*/M_\odot > 10.2$ start to be classified as composite objects (where both photoionization by stars and nuclear activity contribute to produce the emission lines). They are placed in the AGN region of the diagnostic diagrams for the highest masses considered in our sample.
- At fixed redshift, the classification of the stacked spectra displays a trend with increasing stellar mass. The general trend follows the left branch of the SDSS classification to the bulk of the star-forming galaxy population. At the highest stellar masses, the tracks fall in the composite and then in the AGN region. This is visible in the [NII] and in the MEx diagram, whereas it is not well observed in the [OII] diagram.
- The MEx diagram represents a useful tool for investigating the ionizing mechanisms inside galaxies, especially at high redshift. The Lamareille (2010) [OII] diagram is not as effective because of the ambiguity between star-forming, composites, and Seyfert 2 galaxies in some regions of the diagram.

Moreover, it is necessary to be in a specific redshift interval to measure all involved emission lines. The confusion that this diagram shows can be due to its higher sensitivity to shocks than to AGN photoionization.

- While there is no clear trend with redshift on the low-redshift BPT diagram, there is a trend on the MEx diagram when combining the low- and high-redshift bins. The high-redshift stacks display clearly more composite- and AGN-like spectra. However, the explanation of this trend (higher AGN-detection rate at higher redshift) may include true evolutionary effects as well as selection biases.
- The link between stellar population age and galaxy stellar mass, combined with the increasing AGN-detection rate for increasing mass and redshift, is consistent with a scenario where AGN could act to quench the star formation and then contribute to the transformation from young blue late-type galaxies to old red early-type galaxies.

Acknowledgements. The authors thank the anonymous referee for very useful comments and suggestions that helped to improve the paper. M. Vitale is also grateful to M. García-Marín, M. Valencia-S., M. Bremer, and A. Eckart for their advice and support. M. Vitale is member of the International Max-Planck Research School (IMPRS) for Astronomy and Astrophysics at the Universities of Bonn and Cologne, supported by the Max-Planck Society. This research is based on observations undertaken at the European Southern Observatory (ESO) Very Large Telescope (VLT) under the Large Program 175.A-0839.

References

- Aird, J., Coil, A. L., Moustakas, J., et al. 2012, *ApJ*, 746, 90
- Asari, N. V., Cid Fernandes, R., Stasińska, G., et al. 2007, *MNRAS*, 381, 263
- Baldry, I. K., Glazebrook, K., Brinkmann, J., et al. 2004, *ApJ*, 600, 681
- Baldwin, J. A., Phillips, M. M., & Terlevich, R. 1981, *PASP*, 93, 5
- Balogh, M. L., Baldry, I. K., Nichol, R., et al. 2004, *ApJ*, 615, L101
- Bauer, F. E., Alexander, D. M., Brandt, W. N., et al. 2004, *AJ*, 128, 2048
- Bell, E. F., Zheng, X. Z., Papovich, C., et al. 2007, *ApJ*, 663, 834
- Bertoldi, F., Carilli, C., Aravena, M., et al. 2007, *ApJS*, 172, 132
- Binney, J. 2004, in *The Riddle of Cooling Flows in Galaxies and Clusters of galaxies*, eds. T. Reiprich, J. Kempner, & N. Soker, 233
- Bolzonella, M., Kovač, K., Pozzetti, L., et al. 2010, *A&A*, 524, A76
- Bongiorno, A., Mignoli, M., Zamorani, G., et al. 2010, *A&A*, 510, A56
- Brandt, W. N., & Alexander, D. M. 2010, *Proc. National Acad. Sci.*, 107, 7184
- Brandt, W. N., & Hasinger, G. 2005, *ARA&A*, 43, 827
- Brusa, M., Civano, F., Comastri, A., et al. 2010, *ApJ*, 716, 348
- Bruzual, G., & Charlot, S. 2003, *MNRAS*, 344, 1000
- Bundy, K., Fukugita, M., Ellis, R. S., Kodama, T., & Conselice, C. J. 2004, *ApJ*, 601, L123
- Bundy, K., Ellis, R. S., Conselice, C. J., et al. 2006, *ApJ*, 651, 120
- Calzetti, D., Kinney, A. L., & Storchi-Bergmann, T. 1994, *ApJ*, 429, 582
- Capak, P., Aussel, H., Ajiki, M., et al. 2007, *ApJS*, 172, 99
- Caputi, K. I., Lilly, S. J., Aussel, H., et al. 2008, *ApJ*, 680, 939
- Caputi, K. I., Lilly, S. J., Aussel, H., et al. 2009, *ApJ*, 707, 1387
- Cattaneo, A., Faber, S. M., Binney, J., et al. 2009, *Nature*, 460, 213
- Chabrier, G. 2003, *ApJ*, 586, L133
- Ciotti, L., & Ostriker, J. P. 1997, *ApJ*, 487, L105
- Comastri, A., & Brusa, M. 2008, *Astron. Nachr.*, 329, 122
- Conselice, C. J., Bundy, K., Trujillo, I., et al. 2007, *MNRAS*, 381, 962
- Cooper, M. C., Newman, J. A., Weiner, B. J., et al. 2008, *MNRAS*, 383, 1058
- Cowie, L. L., Songaila, A., Hu, E. M., & Cohen, J. G. 1996, *AJ*, 112, 839
- Croton, D. J., Springel, V., White, S. D. M., et al. 2006, *MNRAS*, 365, 11
- Daddi, E., Dickinson, M., Chary, R., et al. 2005, *ApJ*, 631, L13
- Dopita, M. A., Kewley, L. J., & Sutherland, R. S. 2002, in *Rev. Mex. Astron. Astrofis.* 12, eds. W. J. Henney, J. Franco, & M. Martos, 225
- Faber, S. M., Willmer, C. N. A., Wolf, C., et al. 2007, *ApJ*, 665, 265
- Ferrarese, L., & Merritt, D. 2000, *ApJ*, 539, L9
- Filippenko, A. V., & Ho, L. C. 2003, *ApJ*, 588, L13
- Garn, T., & Best, P. N. 2010, *MNRAS*, 409, 421
- Hasinger, G., Cappelluti, N., Brunner, H., et al. 2007, *ApJS*, 172, 29
- Heavens, A., Panter, B., Jimenez, R., & Dunlop, J. 2004, *Nature*, 428, 625
- Heckman, T. M. 1980, *A&A*, 87, 152
- Ho, L. C. 2005, *ApJ*, 629, 680
- Ho, L. C., Filippenko, A. V., & Sargent, W. L. W. 1997a, *ApJ*, 487, 568
- Ho, L. C., Filippenko, A. V., & Sargent, W. L. W. 1997b, *ApJ*, 487, 568
- Hogg, D. W., Blanton, M. R., Brinchmann, J., et al. 2004, *ApJ*, 601, L29
- Hopkins, P. F., Hernquist, L., Cox, T. J., et al. 2006, *ApJS*, 163, 1
- Ilbert, O., Capak, P., Salvato, M., et al. 2009, *ApJ*, 690, 1236
- Ivezić, Ž., Menou, K., Knapp, G. R., et al. 2002, *AJ*, 124, 2364
- Jimenez, R., Panter, B., Heavens, A. F., & Verde, L. 2005, *MNRAS*, 356, 495
- Juneau, S., Glazebrook, K., Crampton, D., et al. 2005, *ApJ*, 619, L135
- Juneau, S., Dickinson, M., Alexander, D. M., & Salim, S. 2011, *ApJ*, 736, 104
- Kauffmann, G., Heckman, T. M., Tremonti, C., et al. 2003, *MNRAS*, 346, 1055
- Kewley, L. J., Dopita, M. A., Sutherland, R. S., Heisler, C. A., & Trevena, J. 2001, *ApJ*, 556, 121
- Kewley, L. J., Geller, M. J., & Jansen, R. A. 2003, in *BAAS Meeting Abstracts*, 35, 119.01
- Kewley, L. J., Groves, B., Kauffmann, G., & Heckman, T. 2006, *MNRAS*, 372, 961
- Kodama, T., Yamada, T., Akiyama, M., et al. 2004, *MNRAS*, 350, 1005
- Koekemoer, A. M., Aussel, H., Calzetti, D., et al. 2007, *ApJS*, 172, 196
- Lamareille, F. 2010, *A&A*, 509, A53
- Lamareille, F., Mouhcine, M., Contini, T., Lewis, I., & Maddox, S. 2004, *MNRAS*, 350, 396
- Lequeux, J., Peimbert, M., Rayo, J. F., Serrano, A., & Torres-Peimbert, S. 1979, *A&A*, 80, 155
- Lilly, S. J., Le Fèvre, O., Renzini, A., et al. 2007, *ApJS*, 172, 70
- Lilly, S. J., Le Brun, V., Maier, C., et al. 2009, *ApJS*, 184, 218
- Magorrian, J., Tremaine, S., Richstone, D., et al. 1998, *AJ*, 115, 2285
- Maiolino, R., Nagao, T., Grazian, A., et al. 2008, *A&A*, 488, 463
- Martig, M., Bournaud, F., Teyssier, R., & Dekel, A. 2009, *ApJ*, 707, 250
- McCracken, H. J., Capak, P., Salvato, M., et al. 2010, *ApJ*, 708, 202
- Miller, C. J., Nichol, R. C., Gómez, P. L., Hopkins, A. M., & Bernardi, M. 2003, *ApJ*, 597, 142
- Narayanan, D., Cox, T. J., Shirley, Y., et al. 2008, *ApJ*, 684, 996
- Osterbrock, D. E. 1989, *Astrophysics of gaseous nebulae and active galactic nuclei*
- Padovani, P., & Urry, C. M. 1992, *ApJ*, 387, 449
- Pérez-González, P. G., Rieke, G. H., Villar, V., et al. 2008, *ApJ*, 675, 234
- Pérez-Montero, E., Hägele, G. F., Contini, T., & Díaz, Á. I. 2007, *MNRAS*, 381, 125
- Pozzetti, L., Bolzonella, M., Zucca, E., et al. 2010, *A&A*, 523, A13
- Richstone, D., Ajhar, E. A., Bender, R., et al. 1998, *Nature*, 395, A14
- Rola, C. S., Terlevich, E., & Terlevich, R. J. 1997, *MNRAS*, 289, 419
- Sanders, D. B., Soifer, B. T., Elias, J. H., Neugebauer, G., & Matthews, K. 1988, *ApJ*, 328, L35
- Sanders, D. B., Salvato, M., Aussel, H., et al. 2007, *ApJS*, 172, 86
- Sarzi, M., Rix, H.-W., Shields, J. C., et al. 2005, *ApJ*, 628, 169
- Savaglio, S., Glazebrook, K., Le Borgne, D., et al. 2005, *ApJ*, 635, 260
- Schawinski, K., Thomas, D., Sarzi, M., et al. 2007, *MNRAS*, 382, 1415
- Schawinski, K., Urry, C. M., Virani, S., et al. 2010, *ApJ*, 711, 284
- Schinnerer, E., Smolčić, V., Carilli, C. L., et al. 2007, *ApJS*, 172, 46
- Scoville, N., Aussel, H., Brusa, M., et al. 2007, *ApJS*, 172, 1
- Shields, J. C., Rix, H.-W., Sarzi, M., et al. 2007, *ApJ*, 654, 125
- Silk, J. 2005, *MNRAS*, 364, 1337
- Silk, J., & Rees, M. J. 1998, *A&A*, 331, L1
- Silverman, J. D., Lamareille, F., Maier, C., et al. 2009, *ApJ*, 696, 396
- Springel, V., Di Matteo, T., & Hernquist, L. 2005, *ApJ*, 620, L79
- Stasińska, G., Cid Fernandes, R., Mateus, A., Sodr , L., & Asari, N. V. 2006, *MNRAS*, 371, 972
- Strateva, I., Ivezić, Ž., Knapp, G. R., et al. 2001, *AJ*, 122, 1861
- Tanaka, M., Kodama, T., Arimoto, N., et al. 2005, *MNRAS*, 362, 268
- Taniguchi, Y., Scoville, N., Murayama, T., et al. 2007, *ApJS*, 172, 9
- Thomas, D., Maraston, C., Bender, R., & Mendes de Oliveira, C. 2005, *ApJ*, 621, 673
- Tremonti, C. A., Heckman, T. M., Kauffmann, G., et al. 2004, *ApJ*, 613, 898
- Tresse, L., Rola, C., Hammer, F., et al. 1996, *MNRAS*, 281, 847
- Treu, T., Ellis, R. S., Liao, T. X., & van Dokkum, P. G. 2005, *ApJ*, 622, L5
- van der Wel, A., Franx, M., van Dokkum, P. G., et al. 2005, *ApJ*, 631, 145
- Veilleux, S., & Osterbrock, D. E. 1987, *ApJS*, 63, 295
- Vitale, M., Zuther, J., García-Marín, M., et al. 2012, *A&A*, 546, A17
- Worthey, G. 1994, *ApJS*, 95, 107

Appendix A

Here we present the zCOSMOS stacked spectra that were in our study.

For a fixed redshift, the stacked spectra – before stellar continuum subtraction – show a [OIII] line whose strength decreases with the progressive increase of the stellar mass (Fig. A.1), especially if compared with the $H\beta$ line. The latter shows a weakening as well. The $H\alpha$ line is very strong at low masses. The intensity of the [NII] and $H\alpha$ decreases up to the point at the highest mass bin where these lines show the same intensity. In Fig. A.2, the [OIII] and $H\beta$ lines show the same trend as at lower redshifts. The [OII] line intensity decreases with the increase of the mass, but it is always the strongest line in the high-redshift composite spectra.

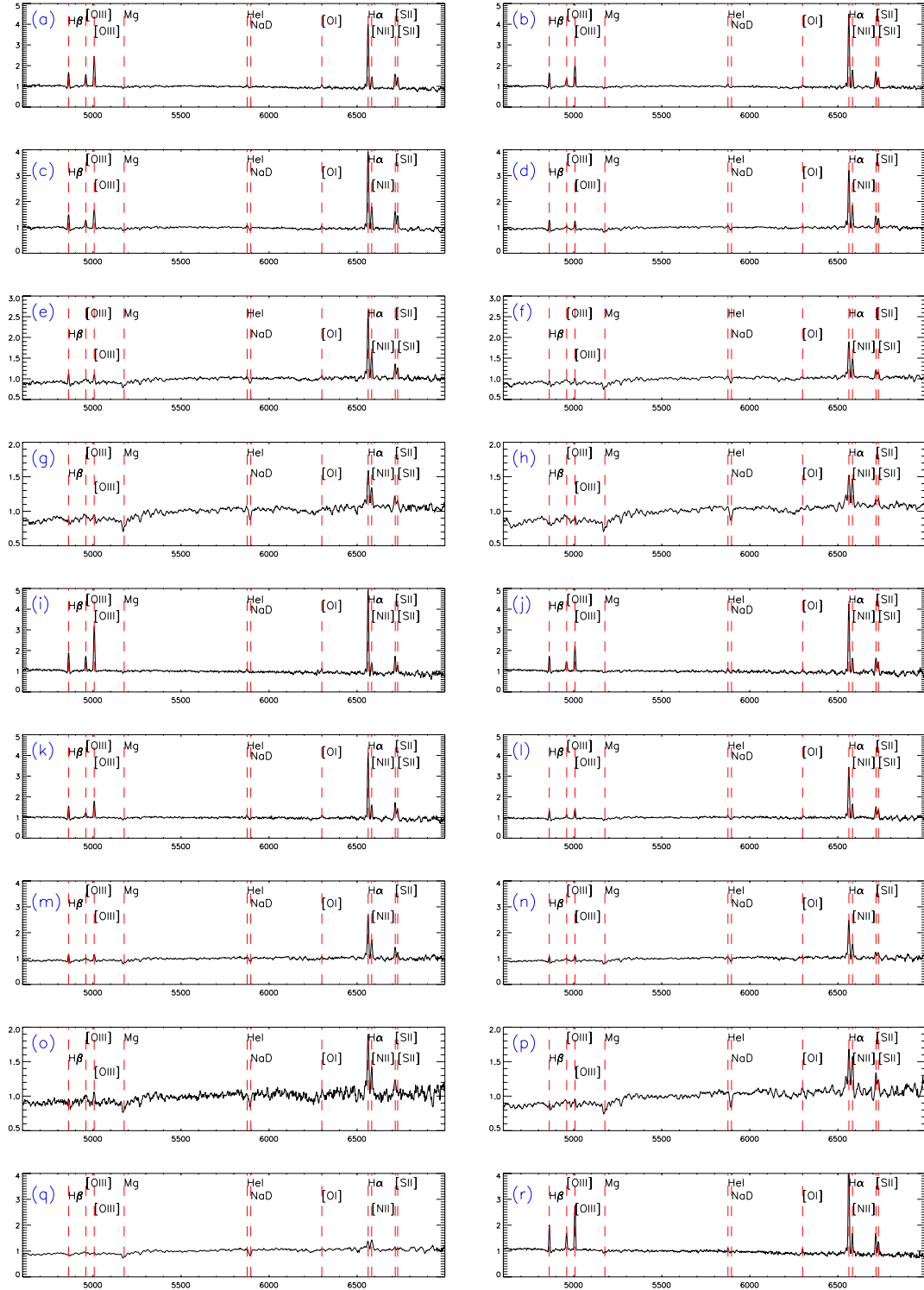


Fig. A.1. Stacked zCOSMOS spectra at lower z . Bin $9.25 \leq \log M_*/M_\odot < 9.5$, $0.177 \leq z < 0.242$ (panel **a**); $9.5 \leq \log M_*/M_\odot < 9.75$, $0.177 \leq z < 0.242$ (panel **b**); $9.75 \leq \log M_*/M_\odot < 10$, $0.177 \leq z < 0.242$ (panel **c**); $10 \leq \log M_*/M_\odot < 10.25$, $0.177 \leq z < 0.242$ (panel **d**); $10.25 \leq \log M_*/M_\odot < 10.5$, $0.177 \leq z < 0.242$ (panel **e**); $10.5 \leq \log M_*/M_\odot < 10.75$, $0.177 \leq z < 0.242$ (panel **f**); $10.75 \leq \log M_*/M_\odot < 11$, $0.177 \leq z < 0.242$ (panel **g**); $9 \leq \log M_*/M_\odot < 9.25$, $0.242 \leq z < 0.306$ (panel **h**); $9.25 \leq \log M_*/M_\odot < 9.5$, $0.242 \leq z < 0.306$ (panel **i**); $9.5 \leq \log M_*/M_\odot < 9.75$, $0.242 \leq z < 0.306$ (panel **j**); $9.75 \leq \log M_*/M_\odot < 10$, $0.242 \leq z < 0.306$ (panel **k**); $10 \leq \log M_*/M_\odot < 10.25$, $0.242 \leq z < 0.306$ (panel **l**); $10.25 \leq \log M_*/M_\odot < 10.5$, $0.242 \leq z < 0.306$ (panel **m**); $10.5 \leq \log M_*/M_\odot < 10.75$, $0.242 \leq z < 0.306$ (panel **n**); $10.75 \leq \log M_*/M_\odot < 11$, $0.242 \leq z < 0.306$ (panel **o**); $11 \leq \log M_*/M_\odot < 11.25$, $0.242 \leq z < 0.306$ (panel **p**); $9.25 \leq \log M_*/M_\odot < 9.5$, $0.306 \leq z < 0.371$ (panel **q**); $9.5 \leq \log M_*/M_\odot < 9.75$, $0.306 \leq z < 0.371$ (panel **r**); $9.75 \leq \log M_*/M_\odot < 10$, $0.306 \leq z < 0.371$ (panel **s**); $10 \leq \log M_*/M_\odot < 10.25$, $0.306 \leq z < 0.371$ (panel **t**); $10.25 \leq \log M_*/M_\odot < 10.5$, $0.306 \leq z < 0.371$ (panel **u**); $10.5 \leq \log M_*/M_\odot < 10.75$, $0.306 \leq z < 0.371$ (panel **v**); $10.75 \leq \log M_*/M_\odot < 11$, $0.306 \leq z < 0.371$ (panel **w**); $11 \leq \log M_*/M_\odot < 11.25$, $0.306 \leq z < 0.371$ (panel **x**); $9.25 \leq \log M_*/M_\odot < 9.5$, $0.371 \leq z \leq 0.436$ (panel **y**); $9.5 \leq \log M_*/M_\odot < 9.75$, $0.371 \leq z \leq 0.436$ (panel **z**); $9.75 \leq \log M_*/M_\odot < 10$, $0.371 \leq z \leq 0.436$ (panel **a2**); $10 \leq \log M_*/M_\odot < 10.25$, $0.371 \leq z \leq 0.436$ (panel **c2**); $10.25 \leq \log M_*/M_\odot < 10.5$, $0.371 \leq z \leq 0.436$ (panel **d2**); $10.5 \leq \log M_*/M_\odot < 10.75$, $0.371 \leq z \leq 0.436$ (panel **e2**); $10.75 \leq \log M_*/M_\odot < 11$, $0.371 \leq z \leq 0.436$ (panel **f2**); $11 \leq \log M_*/M_\odot < 11.25$, $0.371 \leq z \leq 0.436$ (panel **g2**)).

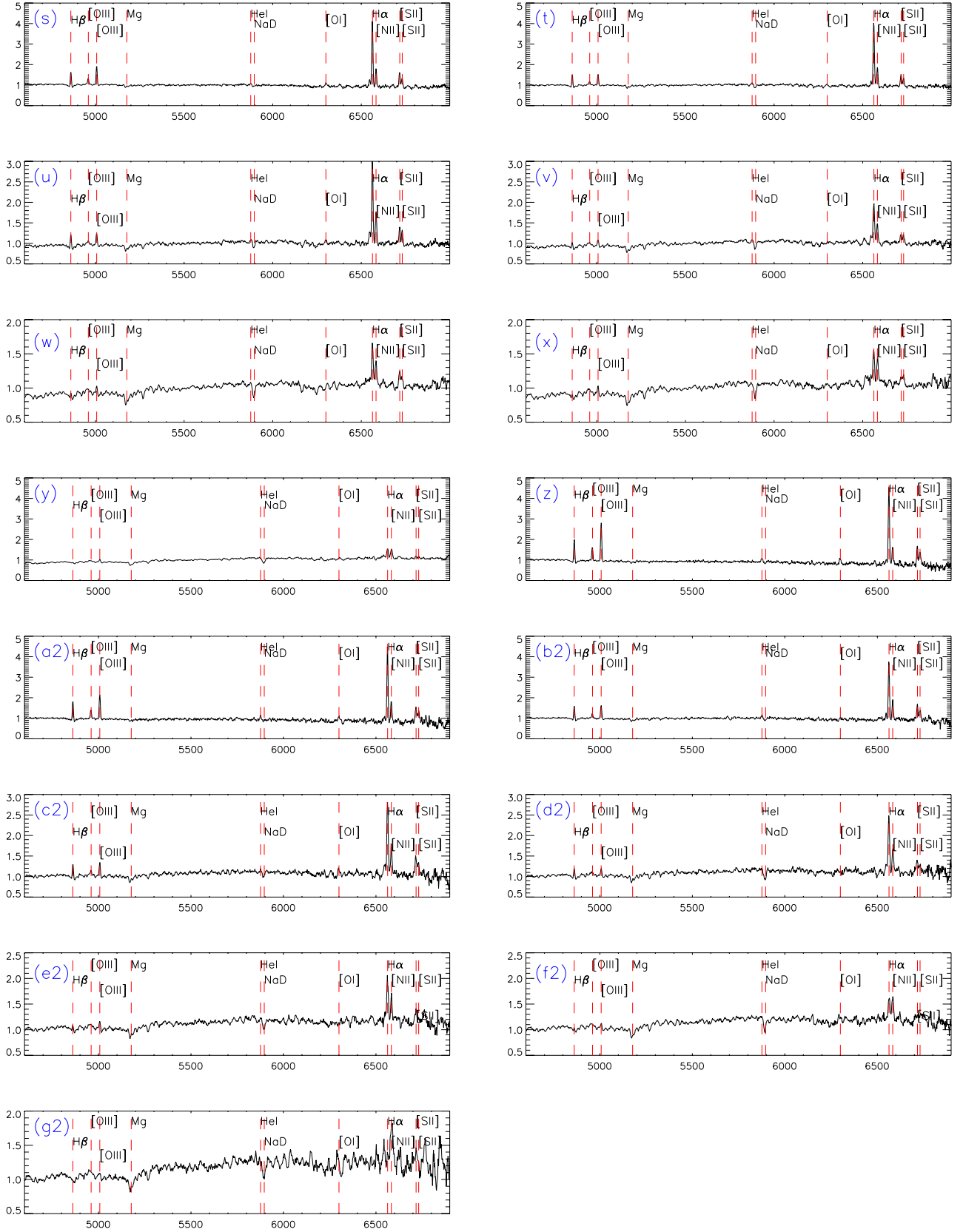


Fig. A.1. continued.

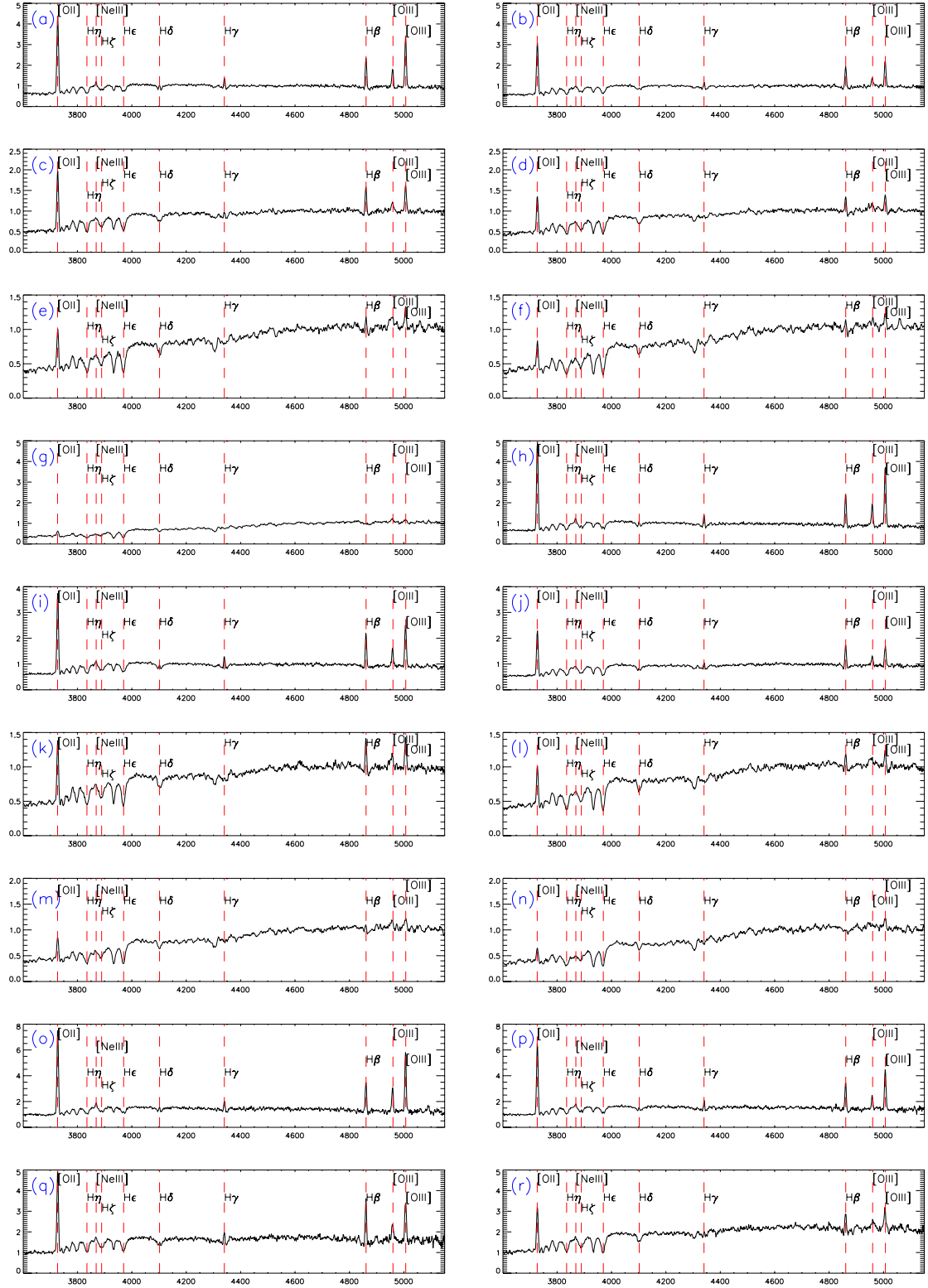


Fig. A.2. Stacked zCOSMOS spectra at higher z . Bin $9.5 \leq \log M_*/M_\odot < 9.75$, $0.548 \leq z < 0.632$ (panel a); $9.75 \leq \log M_*/M_\odot < 10$, $0.548 \leq z < 0.632$ (panel b); $10 \leq \log M_*/M_\odot < 10.25$, $0.548 \leq z < 0.632$ (panel c); $10.25 \leq \log M_*/M_\odot < 10.5$, $0.548 \leq z < 0.632$ (panel d); $10.5 \leq \log M_*/M_\odot < 10.75$, $0.548 \leq z < 0.632$ (panel e); $10.75 \leq \log M_*/M_\odot < 11$, $0.548 \leq z < 0.632$ (panel f); $11 \leq \log M_*/M_\odot < 11.25$, $0.548 \leq z < 0.632$ (panel g); $9.5 \leq \log M_*/M_\odot < 9.75$, $0.632 \leq z < 0.716$ (panel h); $9.75 \leq \log M_*/M_\odot < 10$, $0.632 \leq z < 0.716$ (panel i); $10 \leq \log M_*/M_\odot < 10.25$, $0.632 \leq z < 0.716$ (panel j); $10.25 \leq \log M_*/M_\odot < 10.5$, $0.632 \leq z < 0.716$ (panel k); $10.5 \leq \log M_*/M_\odot < 10.75$, $0.632 \leq z < 0.716$ (panel l); $10.75 \leq \log M_*/M_\odot < 11$, $0.632 \leq z < 0.716$ (panel m); $11 \leq \log M_*/M_\odot < 11.25$, $0.632 \leq z < 0.716$ (panel n); $9.5 \leq \log M_*/M_\odot < 9.75$, $0.716 \leq z < 0.8$ (panel o); $9.75 \leq \log M_*/M_\odot < 10$, $0.716 \leq z < 0.8$ (panel p); $10 \leq \log M_*/M_\odot < 10.25$, $0.716 \leq z < 0.8$ (panel q); $10.25 \leq \log M_*/M_\odot < 10.5$, $0.716 \leq z < 0.8$ (panel r); $10.5 \leq \log M_*/M_\odot < 10.75$, $0.716 \leq z < 0.8$ (panel s); $10.75 \leq \log M_*/M_\odot < 11$, $0.716 \leq z < 0.8$ (panel t); $11 \leq \log M_*/M_\odot < 11.25$, $0.716 \leq z < 0.8$ (panel u); $9.5 \leq \log M_*/M_\odot < 9.75$, $0.8 \leq z \leq 0.884$ (panel v); $9.75 \leq \log M_*/M_\odot < 10$, $0.8 \leq z \leq 0.884$ (panel w); $10 \leq \log M_*/M_\odot < 10.25$, $0.8 \leq z \leq 0.884$ (panel x); $10.25 \leq \log M_*/M_\odot < 10.5$, $0.8 \leq z \leq 0.884$ (panel y); $10.5 \leq \log M_*/M_\odot < 10.75$, $0.8 \leq z \leq 0.884$ (panel z); $10.75 \leq \log M_*/M_\odot < 11$, $0.8 \leq z \leq 0.884$ (panel a2)); $11 \leq \log M_*/M_\odot < 11.25$, $0.8 \leq z \leq 0.884$ (panel b2)).

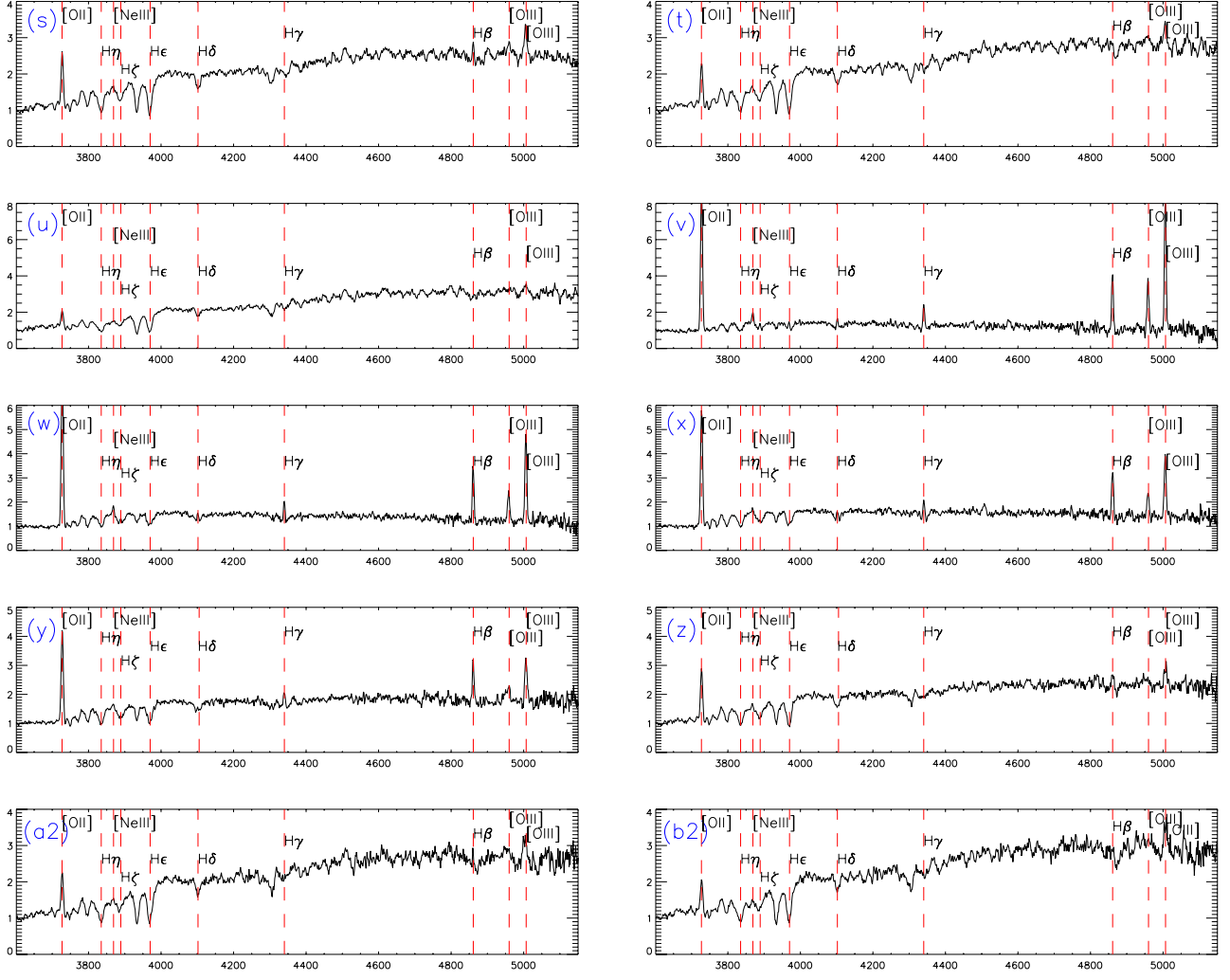


Fig. A.2. continued.

Appendix B

We used the dust-corrected flux ratios for $[\text{OII}]/\text{H}\beta$ instead of the EW ratios originally used by [Lamareille \(2010\)](#).

This appendix (Fig. B.1) shows that the dust-corrected fluxes correspond well enough to the EWs for a sample of SDSS galaxies ([Vitale et al. 2012](#)), especially in the regions occupied by our sample. Hence we can use the original demarcation lines from [Lamareille \(2010\)](#). However, the dust-corrected flux ratios span a slightly more restricted range of $[\text{OIII}]/\text{H}\beta$ values than the EW ratios.

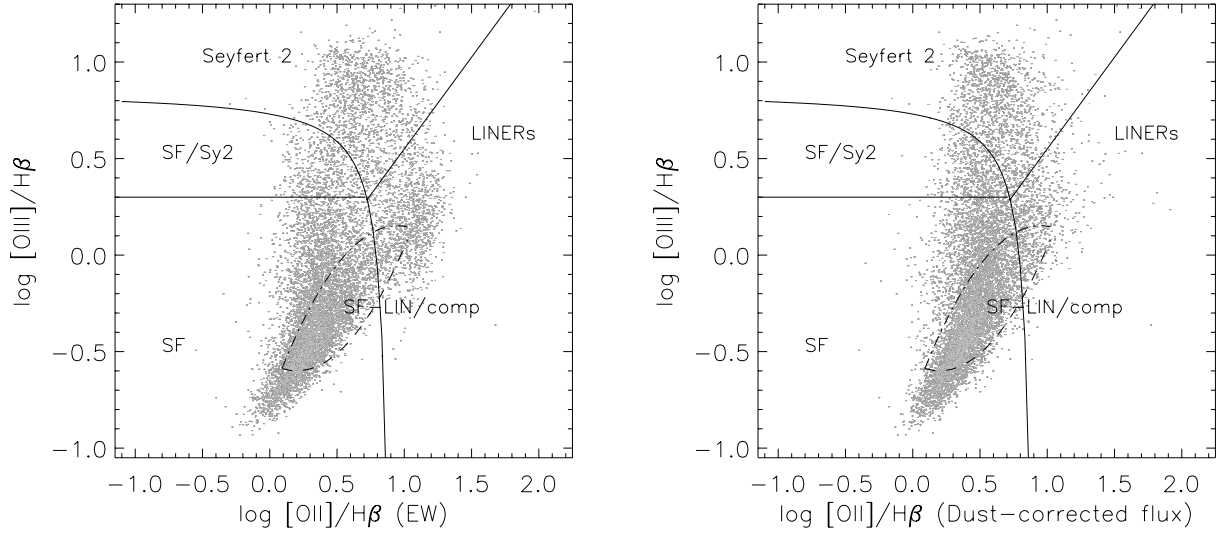


Fig. B.1. $[\text{OII}]$ diagnostic diagram showing the consistency between EW measurements (*left panel*) and dust-corrected fluxes (*right panel*). The solid demarcation lines are taken from [Lamareille \(2010\)](#). The gray distribution represents the SDSS galaxies from [Vitale et al. \(2012\)](#).